Journal of Biomedical Materials Research Part B: Applied Biomaterials

WILEY

Society For Biomaterials

RESEARCH ARTICLE OPEN ACCESS

Bisphosphonate-Modified Polymer-Coated $NaYF_4$:Yb,Er,Pr Upconverting Nanoparticles for Cell Imaging: Synthesis, Physicochemical Characterization and Biosafety

Taras Vasylyshyn[1] | Vitalii Patsula[1] | Oleksandr Shapoval[1] | Ognen Pop-Georgievski[1] | Solomiya Paryzhak[2] | Tetiana Dumych[2] | Victoria Serhiyenko[2] | Nadia Skorokhyd[3] | Olga Klyuchivska[3] | Rafał Konefał[1] | Jiřina Hromádková[1] | Lucia Machová Urdziková[4] | Dana Mareková[4] | Aleš Benda[5] | Pavla Jendelová[4] | Rostyslav Stoika[3,6] | Daniel Horák[1]

[1]Institute of Macromolecular Chemistry, Czech Academy of Sciences, Prague, Czech Republic | [2]Danylo Halytsky Lviv National Medical University, Lviv, Ukraine | [3]Institute of Cell Biology, National Academy of Sciences of Ukraine, Lviv, Ukraine | [4]Institute of Experimental Medicine, Czech Academy of Sciences, Prague, Czech Republic | [5]Faculty of Science of the Charles University, Prague, Czech Republic | [6]Ivan Franko National University of Lviv, Lviv, Ukraine

Correspondence: Daniel Horák (horak@imc.cas.cz)

Received: 7 January 2025 | **Revised:** 17 November 2025 | **Accepted:** 4 December 2025

Keywords: cytotoxicity | hematology parameters | polymer coating | protein corona | upconverting nanoparticles

ABSTRACT

Upconverting nanoparticles (UCNPs) have attracted much attention in nanomedicine due to their ability to upconvert photons. However, their adverse effects hinder the biomedical applications. In this paper, bisphosphonate-modified poly(isobutylene-*alt*-maleic acid)-*graft*-poly(*N,N*-dimethylacrylamide)-coated $NaYF_4$:Yb,Er,Pr UCNPs (UCNP@PIMAPDMA) nanoparticles were designed, which exhibited luminescence emission simultaneously in the visible and NIR-II regions. The developed UCNPs were characterized by a range of physicochemical methods, including transmission electron and energy dispersive microscopy (TEM and EDAX), dynamic light scattering (DLS), X-ray diffraction analysis (XRD), spectrofluorometry, X-ray photoelectron spectroscopy (XPS), and so forth. The UCNP@PIMAPDMA nanoparticles were also evaluated in cell cultures and experimental animals. The particles showed good biocompatibility with cultured human embryonic kidney HEK293 cells commonly used in toxicological studies. Neat UCNPs were cytotoxic towards these cells, which was confirmed by measuring their viability using the 3-(4,5-dimethylthiazol-2-yl)-2,5-diphenyltetrazolium bromide (MTT) colorimetric assay. Blood serum proteins adhered to the surface of UCNP@PIMAPDMA particles, forming a protein corona that may contribute to particle biosafety. After intravenous injection of these particles into laboratory mice, there were no statistically significant changes in body mass of the treated animals. Also, no big adverse effects on blood cell profile, enzymatic and metabolic markers of hepatotoxicity and nephrotoxicity were observed. Finally, the application potential of UCNP@PIMAPDMA nanoparticles was confirmed by successfully imaging the cytoplasm of rat mesenchymal stem cells and rat C6 glioblastoma cells using laser scanning confocal microscopy.

1 | Introduction

Lanthanide-based upconverting nanoparticles (UCNPs) have recently received much attention due to their applicability for bioimaging, biosensing, targeted drug delivery, photodynamic therapy, high-resolution microscopy or the production of printable barcodes, authentication, recycling labels, and so forth [1, 2]. For these applications, particles should meet some important requirements such as uniform size and morphology, crystal phase, chemical composition, and surface chemistry, which affect their

physicochemical properties and thus cell-particle interactions [3]. UCNPs convert near-infrared (NIR) light into higher-energy luminescence photons that exhibit emission bands in the ultraviolet, visible (Vis) and NIR regions with long luminescence lifetimes. They are ideal for optical measurements with low background and high penetration depth in biological systems [4]. The most commonly used crystalline host matrices for these nanoparticles are fluorides such as $NaYF_4$ due to their high transparency, low phonon frequency, high quantum efficiency, and high chemical stability. Doping is often achieved using sensitizer/activator pairs, for example Yb^{3+}/Er^{3+} and Yb^{3+}/Tm^{3+}, which provide efficient green, red and blue emissions [5]. It has also been shown that by doping Pr^{3+} and Yb^{3+} ions into the fluoride matrix, upconversion and downconversion luminescence can be combined, which may be useful for advanced biomedical applications [6, 7]. Here, upconversion emission from the Vis to the deep ultraviolet region (200–280 nm) enables targeted deactivation of various types of microorganisms, including viruses and bacteria, whereas downconversion emission from the NIR-I (700–900 nm) into the NIR-II region (1000–1350 nm) is used for background-free high-contrast optical imaging of deeper biological tissues [8, 9].

Various methods, such as coprecipitation [10], hydro(solvo)thermal [11] and microwave synthesis [12], or thermal decomposition [13], have been developed to synthesize rare-earth-based UCNPs of different sizes, morphologies and architectures. The latter technique is the simplest one for the preparation of monodisperse UCNPs with controlled size and morphology, which can be tuned from nanospheres to hexagonal nanoplates, nanorods and nanoprisms [14]. However, in bioapplications, from diagnosis to disease treatment, the effects of nanoparticles must be predictable and controllable, with minimal cytotoxicity. To meet these requirements, the UCNP surface must be carefully engineered to allow for stabilization, specific targeting and recognition of biochemical species while preventing particle aggregation and dissolution [15]. This can be achieved by coating the particles with a ligand-containing shell or by embedding them in an inorganic or polymeric matrix [16].

There are many suitable polymers for the steric stabilization of particles, the most common being based on poly(ethylene glycol) (PEG) [17, 18] and carbohydrates such as starch, dextran, and chitosan [19–21]. On the other hand, ligands based on small oxygen-, nitrogen-, phosphorus-, or sulfur-containing molecules provide the advantage of a smaller hydrodynamic particle diameter, which is preferred for in vivo applications due to efficient transmembrane permeation [22]. A thin protective layer on UCNPs is often also formed with silica, gold or semiconductors such as zinc sulfide to enhance photoluminescence [23–27]. A hydrophobic surface that allows dispersion of particles in organic solvents can be achieved by coating with long-chain hydrocarbon ligands such as oleic or lauric acid, dodecyl or hexadecyl phosphonate, or dihexadecyl phosphate [28]. Then, polymers such as poly(acrylic acid), poly(methyl methacrylate), polyethyleneimine, polyimidazoles, polystyrene-*block*-poly(acrylic acid), dendrimers, PEG-modified poly(maleic anhydride-*alt*-1-octadecene), or poly(maleic anhydride-*alt*-1-tetradecene) have been used to produce a hydrophilic surface [29–33]. Another example of surface protection of UCNPs is their encapsulation in micelles with a hydrophobic interior consisting of phospholipids [34]. Various molecules of biomedical origin, such as antibodies, peptides, proteins and drugs, have also been conjugated to nanoparticles to enable the diagnosis and therapy of various diseases [35]. For example, $NaYF_4$:Yb^{3+},Er^{3+}-based UCNPs coated with poly(isobutylene-*alt*-maleic anhydride) (PIMA) and functionalized with various phosphonate anchor groups and PEG moieties exhibited high long-term colloidal stability in biologically relevant buffers, allowing their application in bioimaging and nanomedicine [36].

In this paper, a sophisticated bisphosphonate polymer based on poly(isobutylene-*alt*-maleic acid)-*graft*-poly(*N,N*-dimethylacrylamide) (PIMAPDMA) was prepared to protect $NaYF_4$:Yb,Er,Pr UCNPs. The many bisphosphonate groups of the polymer ensured good complexation with the particle surface, leading to good colloidal stability and minimal particle dissolution. Moreover, the polymer contains reactive carboxyl groups that can be used for the possible binding of biologically active molecules. Last but not least, it should be mentioned that the PDMA moiety of the polymer was chosen for its hydrophilicity and biocompatibility. However, the main disadvantage of synthetic polymers is their non-biodegradability, which makes them difficult to eliminate from the body and can potentially lead to adverse effects such as inflammation and tissue damage [37]. To overcome this complication, a disulfide-containing cystamine linker, which is potentially biodegradable, was introduced into PIMAPDMA. Finally, the biocompatibility of UCNP@PIMAPDMA particles, which are designed as a fluorescent marker for imaging in the UV–Vis and NIR-II regions, was verified in in vitro and in vivo experiments.

2 | Experimental

2.1 | Materials

YCl_3, $YbCl_3$, $ErCl_3 \cdot 6H_2O$, $PrCl_3$ hydrate, NH_4F, poly(isobutylene-*alt*-maleic acid) (PIMA; $M_w = 6000$ g/mol), diethyl vinylphosphonate, cystamine dihydrochloride, di-*tert*-butyl dicarbonate, octadec-1-ene, bromotrimethylsilane, *N*-hydroxysuccinimide, *N,N*-dicyclohexylcarbodiimide, *N,N*-dimethylaminopyridine, phosphate-buffered saline (PBS; pH 7.4), Dulbecco's modified Eagle's medium (DMEM) and oleic acid were purchased from Sigma-Aldrich (St. Luis, MO, USA). Artificial lysosomal fluid (ALF; pH 4.5) was prepared according to the literature [38]. *N*-Boc-ethylenediamine (BEA) was from Apollo Scientific (Bredbury, UK). Carboxyl-terminated poly(*N,N*-dimethylacrylamide) (PDMA-C; $M_w = 10{,}000$ g/mol) was prepared by RAFT polymerization as described in a previous report [39]. *Tert*-boc-cystamine was obtained from cystamine dihydrochloride and di-*tert*-butyl dicarbonate according to the literature [40]. The solvents were from LachNer (Neratovice, Czech Republic). Distilled demineralized water (conductivity < 0.1 μS/cm) filtered on a Milli-Q Gradient A10 system (Millipore; Molsheim, France) has been used throughout all experiments.

2.2 | Synthesis of Diethyl (2-Aminoethyl) Amino Bis(Ethyl Phosphonate) (DAP)

Briefly, BEA (1 g; 6.25 mmol) and diethyl vinylphosphonate (2.15 g; 13.1 mmol) were dissolved in water (8.4 mL) and heated at 70°C for 18 h under an argon atmosphere. After that, water

was removed at 50°C on a vacuum rotary evaporator. The resulting *N*-boc-protected diethyl (2-aminoethyl)amino bis(ethyl phosphonate) (Boc-DAP) was purified by column chromatography with methanol/dichloromethane as eluent (1:10 v/v, $R_f = 0.65$). The chemical structure of Boc-DAP was confirmed by ^{1}H NMR spectroscopy (Supporting Information; Figure S1a). Yield: 2.2 g.

The *tert*-boc protecting group was removed by stirring Boc-DAP (1 g; 2 mmol) in 3 M methanolic HCl (15 mL) for 3 h. The reaction mixture was then neutralized by the addition of NaOH to pH 10, the methanol was removed at room temperature (RT) under vacuum and the product was extracted with dichloromethane (2 × 40 mL). The combined organic layers were dried over $MgSO_4$, the solvent was removed at RT on a vacuum rotary evaporator and DAP was dried at RT for 5 h under vacuum (13 Pa). The successful removal of the *tert*-boc protecting group was confirmed by the disappearance of the corresponding peak at 1.45 ppm in ^{1}H NMR spectrum of DAP (Figure S1b). Yield: 0.83 g.

2.3 | Synthesis of Cystamine-Terminated Poly(*N,N*-Dimethylacrylamide)

Briefly, PDMA-C (1 g), *tert*-boc-cystamine (81 mg), *N*-hydroxysuccinimide (59 mg), and *N,N*-dimethylaminopyridine (17 mg) were dissolved in dimethyl sulfoxide/chloroform mixture (17 mL; 1/7.5 v/v), cooled in ice bath to 5°C, the solution of *N,N*-dicyclohexylcarbodiimide (103 mg) in chloroform (3 mL) was added and the mixture was stirred at 5°C for 2 h and at RT for 34 h. Chloroform was removed at 30°C on a vacuum rotary evaporator and the resulting *tert*-boc-cystamine-terminated poly(*N,N*-dimethylacrylamide) was purified on a Sephadex LH-20 column (GE Healthcare Bio-Sciences; Uppsala, Sweden) with methanol as eluent. The presence of the *tert*-boc-cystamine group in the PDMA structure was proved by ^{1}H NMR spectroscopy (Figure S2a). *Tert*-boc protecting groups of the polymer (1.23 g) were removed by hydrolysis using 3 M HCl in methanol (8 mL) at RT for 3 h and the pH was adjusted to 10 by adding solid NaOH. The methanol and water were evaporated at 40°C under vacuum (667 Pa) and the cystamine-terminated poly(*N,N*-dimethylacrylamide), hereafter referred to as PDMA, was dissolved in dichloromethane (50 mL). The solution was then filtered, and the solvent was removed under vacuum at 40°C. ^{1}H NMR spectrum of PDMA confirmed the deprotection of terminal amino groups due to the disappearance of the peak at 1.45 ppm (Figure S2b). Yield: 1.16 g.

2.4 | Synthesis of Bisphosphonate-Modified Poly(Isobutylene-*Alt*-Maleic Acid)-*Graft*-Poly(*N,N*-Dimethylacrylamide) (PIMAPDMA)

Briefly, PIMA (70 mg) and PDMA (590 mg) were dissolved in anhydrous *N,N*-dimethylformamide (DMF; 3 mL) and the solution was heated at 60°C for 1.5 h under an Ar atmosphere. The solution of BEA (27 mg) and DAP (88 mg; Figure 1a) in dry DMF (1 mL) was added and the reaction continued at 60°C for 18 h. The resulting *tert*-boc-PIMAPDMA was purified by dialysis (MWCO = 14,000 g/mol) in water, which was exchanged six times within 30 h, and freeze-dried. According to ^{1}H NMR spectroscopy, the resulting polymer contained 19, 17 and 3 DAP, BEA and PDMA moieties per PIMA chain, respectively (Figure S3a). Finally, ethyl ester groups were removed from *tert*-boc-PIMAPDMA (450 mg) dissolved in dichloromethane (10 mL) using bromotrimethylsilane (1.16 mL) under an Ar atmosphere. The solution was stirred at RT for 24 h, the solvent was removed on a vacuum evaporator and the solid was dissolved in a methanol/water mixture (5 mL; 4/1 v/v) with stirring for 1 h. To remove *tert*-boc groups, a solution of 3 M HCl in methanol (8 mL) was added, the mixture was stirred at RT for 2.5 h, methanol was evaporated under vacuum and the protonated PIMAPDMA copolymer (Figure 1b) was purified on a Sephadex LH-20 column with methanol as eluent. The successful removal of *tert*-boc and ethyl ester groups was confirmed by the disappearance of corresponding peaks at 1.45 and 4.2 ppm in ^{1}H NMR spectrum of PIMAPDMA (Figure S3b). Yield: 390 mg.

2.5 | Synthesis of UCNPs

Briefly, YCl_3 (143 mg; 0.73 mmol), $YbCl_3$ (56 mg; 0.2 mmol), $ErCl_3{\cdot}6H_2O$ (8 mg; 0.02 mmol), and $PrCl_3$ hydrate (12 mg; 0.05 mmol) were dissolved in octadec-1-ene (15 mL) and oleic acid (6 mL) at 180°C for 30 min under an Ar atmosphere. After cooling, a methanolic solution (6 mL) of NaOH (100 mg) and NH_4F (148 mg) was added and the mixture was heated at 300°C for 90 min under magnetic stirring in an Ar atmosphere. The resulting $NaYF_4$:Yb,Er,Pr particles (73, 20, 2, and 5 mol.% of Y, Yb, Er, and Pr, respectively) denoted as UCNPs were separated by centrifugation (3,460 rcf), washed twice with hexane, hexane/ethanol, ethanol, ethanol/water (30ml each) and transferred in water reaching a concentration of 8mg/ml.

2.6 | Modification of UCNPs With PIMAPDMA

A dispersion of UCNPs (20 mg) in water (2.5 mL) was added dropwise to aqueous PIMADMA (40 mg) solution (2.5 mL) at RT under sonication (Bandelin Sonoplus; Berlin, Germany; 20% power). Sonication continued for an additional 1 min and the mixture was stirred at 80°C for 16 h. The resulting UCNP@PIMAPDMA particles were separated by centrifugation (13,170 rcf) for 40 min, washed twice with water (2 mL each) and redispersed in water to a concentration of 4 mg/mL.

2.7 | Physicochemical Characterization of UCNPs

Electron micrographs were taken with a TECNAI Spirit G_2 transmission electron microscope (TEM; FEI; Brno, Czech Republic) equipped with energy dispersive spectroscopy (EDAX; Mahwah, NJ, USA). TEM determined the number-average diameter of particles D_n and dispersity ($Đ = D_v/D_n$, where D_v is the volume-average diameter) by analyzing about 300 objects from micrographs. Dynamic light scattering (DLS) was measured using a Zetasizer Ultra instrument (Malvern Instruments; Malvern, UK) to determine the hydrodynamic diameter D_h and polydispersity *PD* of particles in water. Infrared spectra were measured on a 100 T FTIR spectrometer (Perkin-Elmer; Waltham, MA, USA) equipped with a Specac MKII Golden Gate single attenuated total reflection (ATR). Thermogravimetric analysis (TGA) was performed with a PerkinElmer TGA 7 analyzer (Norwalk,

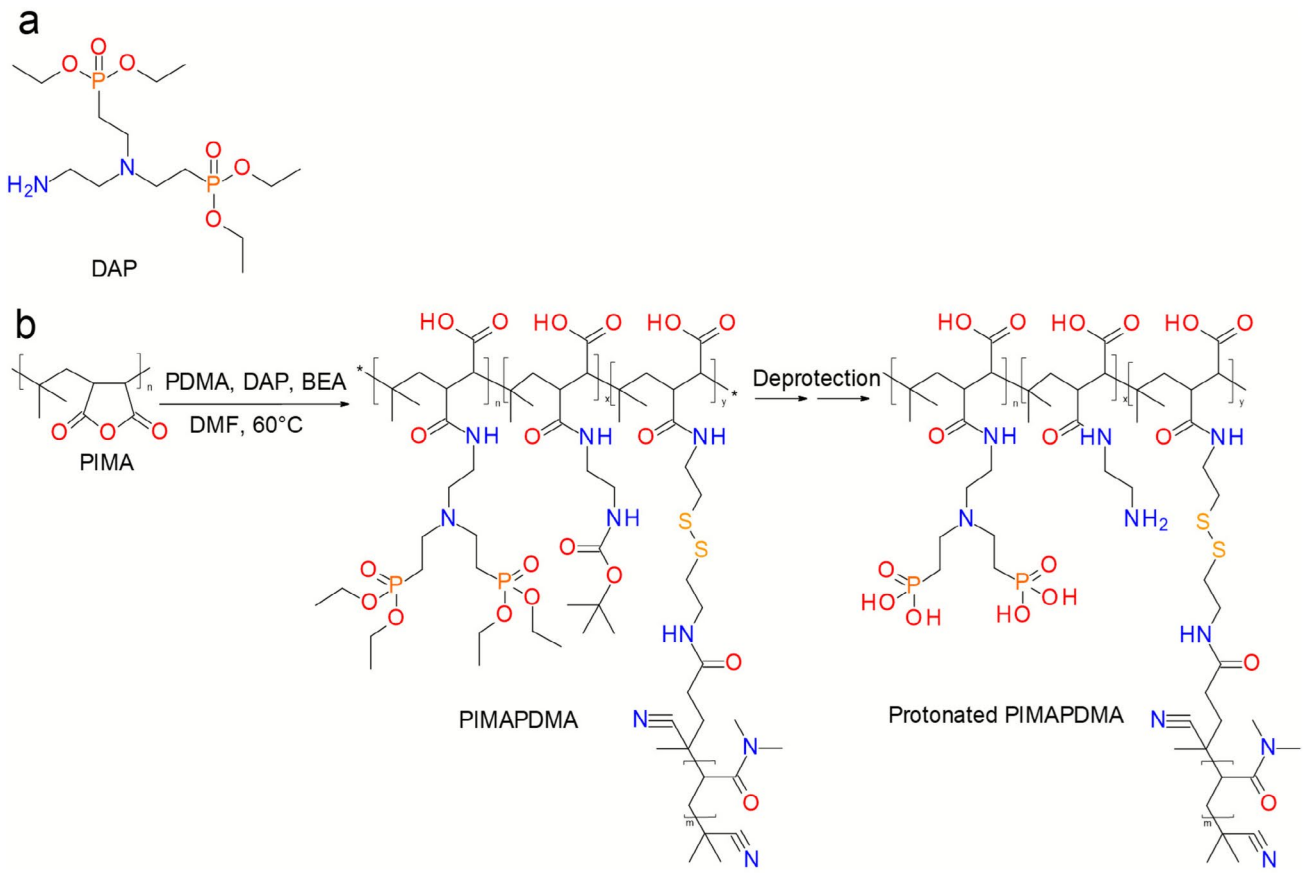

FIGURE 1 | (a) Diethyl (2-aminoethyl)amino bis(ethyl phosphonate) (DAP) and (b) synthesis of protonated bisphosphonate-modified poly(isobutylene-*alt*-maleic acid)-*graft*-poly(*N,N*-dimethylacrylamide) (PIMAPDMA). BEA, *N*-boc-ethylenediamine; DMF, *N,N*-dimethylformamide; PDMA, poly(*N,N*-dimethylacrylamide); PIMA, poly(isobutylene-*alt*-maleic acid).

CT, USA) at 30°C–850°C and a heating rate of 10°C/min in an oxygen atmosphere.

The excitation and emission luminescence spectra at 300–900 nm were measured using a FS5 spectrofluorometer (Edinburgh Instruments; Edinburgh, UK) equipped with pulsed and continuous (150 W) xenon lamps and 980 nm infrared diode lasers with a nominal power of 2 W (MDL-III-980; beam size of $5 \times 8\,mm^2$). Photoluminescence spectra in the NIR-II wavelength region at 900–1300 nm were obtained using a steady-state and time resolved PicoQuant FT-300 spectrofluorometer (Berlin, Germany); a 735 nm laser was used as the pulsed excitation source. X-ray photoelectron spectroscopy (XPS) was performed on a K-Alpha$^+$ XPS spectrometer (Thermo Fisher Scientific; Winsford, UK) operating at a base pressure of 1.0×10^{-7} Pa (details are in Supporting Information).

The phosphorus content was determined as follows. The particles were digested by $HClO_4$ and HNO_3 in a Biotage Initiator microwave reactor (Uppsala, Sweden) and phosphorus content was determined using sulfuric acid, ammonium molybdate, ascorbic acid, and antimony potassium tartrate with an UV–Vis spectrophotometer (Biochrom model Libra S22; Holliston, MA, USA) at 690 nm. Calibration was performed with KH_2PO_4. X-ray diffraction (XRD) patterns of particles were acquired using CuKα radiation (λ 1.54 Å) on a GNR Explorer high-resolution diffractometer (Novara, Italy) with a Mythen 1 K strip detector (STOE; Darmstadt, Germany). Measurements were performed in Bragg–Brentano geometry in the 2Θ range of 2°–70° with a step of 0.05° and a time of 15 s at each step.

2.8 | Colloidal Stability of UCNP@PIMAPDMA Nanoparticles

Neat UCNPs and UCNP@PIMAPDMA particles at a concentration of 1 mg/ml were dispersed in water, 0.01 M PBS (pH 7.4), DMEM with 10% fetal bovine serum and ALF, loaded in 2 ml-plastic vials with a rubber septum and aged at 37°C for 7 days with shaking (250 rpm). The particles were subsequently redispersed in the media in an ultrasonic bath (30 s) and the colloidal stability was determined by DLS by measuring the hydrodynamic size (Dh) and ζ-potential at 25 °C.

2.9 | Degradability of UCNP@PIMAPDMA Nanoparticles

The above-mentioned dispersions of neat UCNP and UCNP@PIMAPDMA nanoparticles were also used for degradability testing. The particles were separated from the medium by centrifugation (14,130 rcf) for 35 min and the resulting supernatants were filtered (MWCO = 30 kg/mol) to remove the remaining particles. The amount of released F^- ions was determined as the molar percentage of F^- (X_F) relative to the amount of fluorine in the $NaYF_4$:Yb,Er,Pr particles using a combined fluoride

electrode (Thermo Fisher Scientific; Waltham, MA, USA) following the manufacturer's protocol.

2.10 | Cell Culture

Human embryonic kidney cells of the HEK293 line were obtained from the Cell Collection of the Institute of Molecular Biology and Genetics of the National Academy of Sciences of Ukraine (Kyiv, Ukraine). Cells were cultured in CELLSTAR plastic dishes (Greiner Bio-One; Kremsmünster, Austria) in DMEM culture medium supplemented with 10% fetal bovine serum (FBS) and 1% penicillin–streptomycin mixture for 24 h in a CO_2-thermostat (BINDER; Tuttlingen, Germany) at 37°C in 5% CO_2 atmosphere and 100% humidity. The nanoparticles or doxorubicin (0.5 μM; Ebewe Pharma; Unterach am Attersee, Austria) were then added to the cultured cells for 48 h for cytotoxicity analyses.

To establish the C6 cell culture, cells of the rat C6 cell line (No 92090409; Sigma-Aldrich) were thawed and rinsed with cold PBS. The cells were then seeded in DMEM medium supplemented with FBS (Merck), primocin and penicillin–streptomycin (Gibco; Life Technologies; Grand Island, NY, USA). Next, neat UCNPs and UCNP@PIMAPDMA nanoparticles (3 mg/mL) were added to C6 cells for 2 days, which were then fixed with paraformaldehyde, stained with 4′,6-diamidin-2-fenylindol (DAPI; Invitrogen; Carlsbad, NM, USA), mounted on microscope slides and visualized by laser scanning microscopy.

Rat mesenchymal stem cells (rMSCs) were obtained by bone marrow aspiration from rat bones. The harvested bone marrow was washed twice with PBS and then cultured in DMEM medium supplemented with FBS, primocin and penicillin–streptomycin at 37°C in a 5% CO_2 atmosphere in a cell culture flask. The culture medium was refreshed twice a week. When cells reached ~70% confluence, they were passaged by treatment with trypsin (Sigma-Aldrich) at 37°C for 4 min, and the trypsin was subsequently neutralized with FBS. Cells were washed with PBS and used in experiments or reseeded for further culture. The rMSCs were incubated with neat UCNPs and UCNP@PIMAPDMA nanoparticles at a concentration of 3 mg/mL for 2 days. After incubation, the cells were fixed with paraformaldehyde, stained with DAPI and mounted on microscope slides for visualization by laser scanning confocal microscopy.

2.11 | In Vitro Cytotoxicity

MTT assay (Sigma-Aldrich) for the determination of mitochondrial dehydrogenase activity and fluorescence microscopy were used to assess the viability of HEK293 cells as previously described [41]. Briefly, cells were placed in wells for 24 h, and nanoparticles or doxorubicin were added for 72 h. MTT reagent dissolved in culture medium (500 μg/mL) was then added to each well with cells and the mixture was incubated at 37°C for 3 h. The MTT-containing medium was removed and the resulting insoluble formazan crystals were dissolved in dimethyl sulfoxide. The absorbance at 490 nm was measured using a BioTek 76,883 Plate Reader multichannel microphotometer (Santa Clara, CA, USA).

2.12 | Detection of Protein Corona

Neat UCNPs and UCNP@PIMAPDMA particles were incubated with FBS (final concentration 50%) at 37°C overnight. Particles were separated by centrifugation (10,000 rcf) for 10 min and washed twice with PBS (pH 7.4). Amido Black 10B solution in 0.5% acetic acid (Carl Roth; Karlsruhe, Germany) was then added and the washing procedure was repeated twice. The particles were resuspended in PBS and the optical density was measured at 490 nm using a BioTek 76,883 Plate Reader multichannel microphotometer.

2.13 | Laser Scanning Confocal Microscopy

Cells were visualized on a Carl Zeiss LSM 880 NLO microscope (Oberkochen, Germany) equipped with a Chameleon Ultra II Ti: sapphire laser (Coherent; Saxonburg, PA, USA) tuned to a wavelength of 975 nm and power adjusted to 100 μW at the sample position. A 40× NA1.1 water immersion objective and a 32 GaAsP array spectral detector covering emission from 410 to 694 nm, operated in single photon counting mode for optimal signal-to-noise ratio, were used. Lambda acquisition mode with full (8.8 nm) spectral resolution was selected to spectrally validate the UCNP emission spectra. Sequential acquisition of frames in channel mode was used for the combined acquisition of differential interference contrast (DIC), DAPI signal and characteristic emission peaks of UCNPs. The first frame was acquired with a 405 nm cw excitation (20 μW on the sample plane), a 410–499 nm fluorescence channel for the DAPI signal, and a transmitted light detector for the DIC. The second frame was excited at 975 nm and detected in two channels: 535–561 nm and 641–686 nm. Since the emission of UCNPs exhibited a very long excited state lifetime in the order of hundreds of microseconds, a fully opened pinhole (300 μm, ~4 Airy units) and the slowest bidirectional scan rate were used, resulting in a typical pixel dwell time of ~50 μs, a pixel size of 90 nm and an image format of 1312×1312 pixels.

2.14 | Animal Study

Male BALB/c mice aged 6–8 weeks with a body mass of 25–30 g were housed in cages equipped with individual filters on an open rack in a room with a 12/12 h cycle of artificial light and darkness at 20°C. Mice were provided with free access to food and water. All procedures were performed in accordance with bioethical standards and with careful attention and responsibility for animal welfare according to the protocol approved by the Bioethics Committee of the Institute of Cell Biology of the National Academy of Sciences of Ukraine (Protocol #1 of July 1, 2023).

For in vivo toxicity determination, mice were divided into two experimental groups of five animals each. Mice were intravenously injected with UCNP@PIMAPDMA particles at a dose of 5 mg/kg and the control group received PBS. The body mass of mice was recorded twice a week for 2 weeks. To evaluate the hematological profile, blood samples were collected from the orbital sinus of anesthetized mice [42]. Blood cells were counted using ethylenediaminotetraacetic acid (EDTA; Sigma-Aldrich) as an anticoagulant. Blood serum was separated by centrifugation and stored at −20°C until use (no longer than 1 week). Hematological

parameters were determined using a DYMIND DF-51 automatic hematology analyzer (5-Part; Dhaka, Bangladesh). Whole blood samples were prepared using EDTA and examined within 2 h of collection at RT.

To measure biochemical parameters in blood serum, such as aspartate aminotransferase (AST), alanine aminotransferase (ALT), alkaline phosphatase (ALP), creatinine, and urea, a semi-automatic chemistry analyzer BS3000M (Wincom; Hunan, China) was used.

Statistical analyses were performed using the Prism 9.5.1 software (GraphPad; Boston, MA, USA). Data were presented as mean ± standard deviation. The one-way ANOVA test and unpaired *t*-test were used to determine statistically significant differences. Significance levels were indicated by the asterisks: $^{*}p < 0.05$, $^{**}p < 0.01$, $^{***}p < 0.001$, and $^{****}p < 0.0001$.

3 | Results and Discussion

3.1 | Synthesis of UCNPs and Their Luminescence

$NaYF_4$(73 mol% Y):Yb(20 mol%),Er(2 mol%),Pr(5 mol%) nanoparticles (UCNPs) were obtained by oleic acid-stabilized high-temperature coprecipitation of the corresponding lanthanide chlorides in octadec-1-ene. The Pr dopant was chosen to enable particle detection in both visible and NIR light. Careful washing of the particles with hexane, ethanol and water allowed their transfer into water. TEM micrographs showed uniform UCNPs of spherical-like shape with a diameter of 32 nm and dispersity $Đ = 1.01$ (Figure 2a). EDAX analysis revealed the elements present in the UCNPs, that is Na (8.1 wt%), Y (21.1 wt%), F (44.4 wt%), Yb (16.7 wt%), Er (2.6 wt%), and Pr (7.0 wt%) (Figure 2c), which only roughly agreed with the theoretical lanthanide content in the particles (Na 11.0, Y 31.1, F 36.4, Yb 16.6, Er 1.6, and Pr 3.4 wt%). The discrepancies could be caused by the fact that EDAX measures surface composition rather than bulk. In addition, the EDAX results indicated the presence of silicon impurity, air oxygen and nitrogen, as well as carbon and copper from the TEM grid. DLS measurements in water determined $D_h = 164$ nm, polydispersity $PD = 0.13$, confirming the narrow particle size distribution, and ζ-potential = 32 mV (Table 1). Concerning the hydrodynamic size of particles in water, it is common for D_h from DLS to be larger than D_n of dry particles according to TEM for several reasons. Although the former technique is based on particle diffusion and provides the *z*-average as a harmonically weighted mean of intensity proportional to the sixth power of the particle radius, TEM image analysis provides a true picture of individual particles and gives the number-average value (D_n) or volume-averaged diameter (D_v); moreover, partial aggregation of particles in water cannot be neglected. The positive ζ-potential of the particles was then derived from metallic ions on the particle surface. The highly crystalline structure of UCNPs measured by an XRD technique demonstrated the main intense peaks at $2\theta = 17.13°$, 29.91°, 30.78°, 43.46°, and 53.67° corresponding to (100), (110), (101), (201), and (211) reflection planes, respectively (Figure 2d). All the peaks were indexed to the standard hexagonal β-phase of $NaYF_4$ (JCPDS card no. 28–1192). Doping Pr^{3+} ions did not lead to the formation of other phases.

The upconversion luminescence of the UCNPs was determined at 980 nm excitation and 2 W/cm^2 (Figure 3a). The particles exhibited characteristic emissions at 407 nm ($^2H_{9/2} \rightarrow {}^4I_{15/2}$), 525 nm ($^2H_{11/2} \rightarrow {}^4I_{15/2}$), 542 nm ($^4S_{3/2} \rightarrow {}^4I_{15/2}$), 654 nm ($^4F_{9/2} \rightarrow {}^4I_{15/2}$) and 803 nm ($^4I_{9/2} \rightarrow {}^4I_{15/2}$), which are typical for Er^{3+} ion transitions in upconverting nanomaterials. Although the upconverting luminescence of Pr^{3+} was weak due to the high probability of non-radiative relaxation inside these ions [43], its upconversion emissions at 486 nm ($^3P_0 \rightarrow {}^3H_4$) and 750 nm ($^3P_0 \rightarrow {}^3F_4$) were observed under 980 nm excitation. After excitation at 495 nm, Pr^{3+} emission at 606 nm appeared in the photoluminescence spectrum of the particles, which was attributed to the $^3P_0 \rightarrow {}^3H_6$ electronic transition (Figure S4). In the excitation spectrum of UCNPs emitted at 606 nm, the peaks from 350 to 500 nm were ascribed to $^4I_{15/2} \rightarrow {}^4G_{11/2}$ (391 nm), $^4I_{15/2} \rightarrow {}^2G_{9/2}$ (418 nm), $^4I_{15/2} \rightarrow {}^4F_{3/2}$ (443 nm) and $^4I_{15/2} \rightarrow {}^4F_{7/2}$ (482 nm) transitions of Er^{3+} and $^3H_4 \rightarrow {}^3P_2$ (443 nm), $^3H_4 \rightarrow {}^3P_1$ (468 nm) and $^3H_4 \rightarrow {}^3P_0$ (495 nm) transitions of Pr^{3+} ions [44]. Furthermore, the UCNPs displayed emission in the NIR-II wavelength region (Figure 3b). The emission at 940 and 1073 nm assigned to the $^3P_0 \rightarrow {}^1G_4$ and $^1D_2 \rightarrow {}^3F_{3,4}$ transition of Pr^{3+} occurred after the absorption of Pr^{3+}photons at 735 nm, which confirms possible excitation of light in both the visible and NIR ranges. This is promising for background-free high-contrast optical imaging of deep biological tissues.

Based on the luminescence measurements, the energy transfer processes in $NaYF_4$:Yb,Er,Pr UCNPs excited at 735 and 980 nm can be interpreted using the energy transfer diagram (Figure 4). Under NIR excitation, the energy transfer and relaxation processes from Yb^{3+} to Er^{3+} (Figure 4; Path I) were identical to those of conventional $NaYF_4$:Yb,Er nanoparticles [46]. At a wavelength of 980 nm, Yb^{3+} absorbed energy and promoted the $^2F_{7/2} \rightarrow {}^2F_{5/2}$ transition. It then resonantly transferred energy to the $^4I_{11/2}$ state of the neighboring Er^{3+} ion due to the matching of excited energy states. This level of the Er^{3+} ion could also be populated by the direct excitation of the Er^{3+} ion from its ground state $^4I_{15/2}$. Thus, Er^{3+} was excited to the higher energy states $^4F_{7/2}$ and ^4G_j (J = 7/2, 9/2, and 11/2) via multiphonon relaxation and energy transfer from Yb^{3+} to Er^{3+}. After the excitation of the $^4F_{7/2}$ level of the Er^{3+} ion, non-radiative relaxation to the $^2H_{11/2}$ and $^4S_{3/2}$ levels occurred. Radiative depopulation of these levels back to the ground state led to green upconversion emissions at 525 and 542 nm corresponding to the $^2H_{11/2} \rightarrow {}^4I_{15/2}$ and $^4S_{3/2} \rightarrow {}^4I_{15/2}$ transitions of the Er^{3+} ion. In addition, an electron from the $^4S_{3/2}$ level of the Er^{3+} ion relaxed non-radiatively to the $^4F_{9/2}$ level, leading to red emission at 654 nm associated with the electronic transition $^4F_{9/2} \rightarrow {}^4I_{15/2}$ of the Er^{3+} ion. The red emission level ($^4F_{9/2}$ of the Er^{3+} ion) was also generated by the energy back-transfer process between ^4G_j (Er^{3+}) and the ground state of Yb^{3+}/Er^{3+} ion [47, 48]. The excited $^4F_{9/2}$ state of the Er^{3+} relaxed non-radiatively to the $^4I_{9/2}$ level and exhibited NIR emission at the $^4I_{9/2} \rightarrow {}^4I_{15/2}$ transition at 803 nm. In addition, the excited state ^4G_j of the Er^{3+} relaxed non-radiatively to the $^2H_{9/2}$ level and exhibited blue emission (407 nm) at the $^2H_{9/2} \rightarrow {}^4I_{15/2}$ transition.

According to the upconversion emission spectra, the energy transfer between the excited Yb^{3+} ions and the neighboring Pr^{3+} ions in $NaYF_4$:Yb,Er,Pr UCNPs was proposed (Figure 4; Path II). The upconversion excitation of the visible emission levels from the excited Pr^{3+} state was achieved due to the low phonon energy and weak lattice field of the fluoride materials [49]. With the excitation wavelength of 980 nm, the population at the $^1G_4$ level of Pr^{3+} could

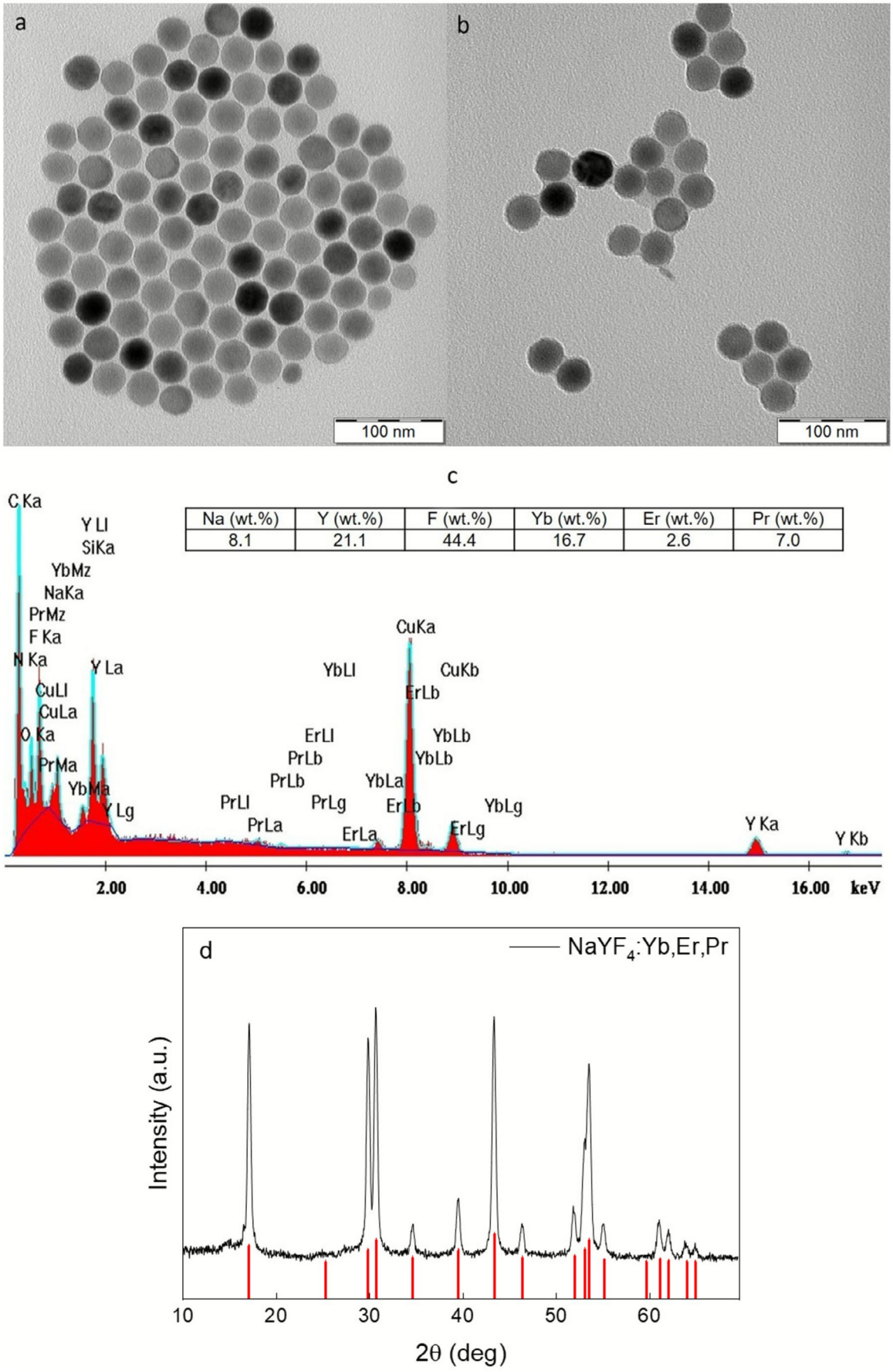

FIGURE 2 | TEM micrographs of (a) $NaYF_4$:Yb,Er,Pr (UCNPs) and (b) UCNP@PIMAPDMA nanoparticles, (c) EDAX analysis and (d) X-ray diffraction pattern of UCNPs; the red vertical lines indicate the standard hexagonal β-phase of $NaYF_4$ (JCPDS card no. 28–1192).

be realized through the absorption of the ground state from $^3H_4$ of Pr^{3+} and the energy transfer from the excited $^2F_{5/2}$ state of Yb^{3+} by the cross-relaxation process [50]. The excited $^1G_4$ state of Pr^{3+} undergoes multiphonon-assisted anti-Stokes absorption of the second photon, which promotes it to the upper emission level $^3P_0$ [51]. The $^3P_0$ level of Pr^{3+} could also be populated by the energy transfer from the two neighboring Yb^{3+} ions. As a result, most of the electrons relaxed into the $^3H_4$ and $^3F_4$ levels, resulting in emission at 486 nm ($^3P_0 \rightarrow {}^3H_4$) and 750 nm ($^3P_0 \rightarrow {}^3F_4$), respectively.

The proposed mechanism of Pr^{3+} emission in the NIR-II wavelength region at 735 nm excitation can be explained as follows. The Pr^{3+} ion in the ground state $^3H_4$ absorbed a photon at 732 nm (Figure 4; Path III) and moved to the excited state $^1D_2$ [52]. This ion relaxed non-radiatively to the lower excited level $^1G_4$ and then was promoted to the upper excited state $^3P_2$ by absorption of the excited state or energy transfer upconversion, where the $^3P_0$ level was populated by non-radiative decay [53, 54]. The $^1D_2$ and $^3P_0$ excited states of Pr^{3+} decayed radiatively to the $^3F_{3,4}$ and $^1G_4$ levels, which showed emission at the $^3P_0 \rightarrow {}^1G_4$ and $^1D_2 \rightarrow {}^1G_4$ transitions, respectively. We note that a detailed study of the energy transfer mechanism in the NIR-II wavelength region of $NaYF_4$:Yb,Er,Pr nanoparticles is beyond the scope of this paper and will be reported elsewhere.

3.2 | Surface Modification of UCNPs With PIMAPDMA and Their Characterization

Bisphosphonate-modified poly(isobutylene-*alt*-maleic acid)-*graft*-poly(*N,N*-dimethylacrylamide) (PIMAPDMA; Figure 1b) was synthesized by nucleophilic addition of maleic anhydride (MA) units of PIMA with amino groups of BEA, DAP and PDMA. PIMA was selected as the basis for PIMAPDMA as an important hydrophobic building block containing 39 MA units. The combination of hydrophobic properties with the high reactivity of MA allows the easy introduction of a large number of bisphosphonate groups, which can interact with the particle surface, thus ensuring good colloidal stability in PBS and minimizing degradation and dissolution [55]. Indeed, it is known that polymers with multiple anchoring groups provide better protection against degradation in aqueous milieu, in contrast to polymers with only one anchoring group. In addition, the highly hydrophilic PDMA sequence of the copolymer promotes biocompatibility and colloidal stability of UCNPs in aqueous solutions [39]. However, the problem with acrylamide- and maleic anhydride-based polymers is their lack of biodegradability. For this reason, a cystamine linker with disulfide bonds was introduced into the PIMAPDMA to enable its degradability in future in vitro and in vivo applications. This is because in the intracellular environment, disulfide groups are cleaved by thiols, such as glutathione, present in cells [56]. This is often exploited for the preparation of various organic and inorganic nanomaterials for biomedical applications [56], where the disulfide bridge of the cysteine linker ensures the degradation of the polymer coating into small fragments ($M_w < 30$ kg/mol) that are excreted from the body by the kidneys. The M_w of synthesized PIMAPDMA according to GPC was 67 kg/mol with a very broad distribution ($Đ = 6.2$), possibly due to the high reactivity and low selectivity of the acylation reaction between MA units and primary amines.

TABLE 1 | Nanoparticle characteristics.

	D_n (nm)	$Đ$	D_h (nm)	PD	ζ-potential (mV)
UCNPs	32	1.01	164	0.13	32
UCNP@PIMAPDMA	41	1.04	156	0.10	−34

Abbreviations: $Đ$, dispersity (TEM); D_h, hydrodynamic diameter (DLS); D_n, number-average particle diameter (TEM); PD, polydispersity (DLS).

The proton signals belonging to *tert*-boc and ethyl protective groups and PDMA in ^{1}H NMR spectrum of *tert*-boc-PIMAPDMA were used to calculate the average number of individual moieties; thus, 19 DAP, 17 BEA and 3 PDMA substituents were determined in the PIMAPDMA (Figure S3a). According to elemental analysis, *tert*-boc-PIMAPDMA contained 0.83 wt% of phosphorus, which represents 13 DAP units. In the FTIR spectrum of PIMAPDMA, the peaks at 912, 1056, 1094 and 1140 cm^{-1} corresponded to the ν(P-OH), symmetric ν_s(P-O) of HPO_3^- group, asymmetric ν_{as}(P-O) of PO_3^{2-} moiety and asymmetric $\nu_{as}(HPO_3^-)$ stretching vibrations, respectively (Figure S5a). These estimative assignments were consistent with the literature [57, 58]. The band at 1255 cm^{-1} was attributed to the δ(NH) bending vibration

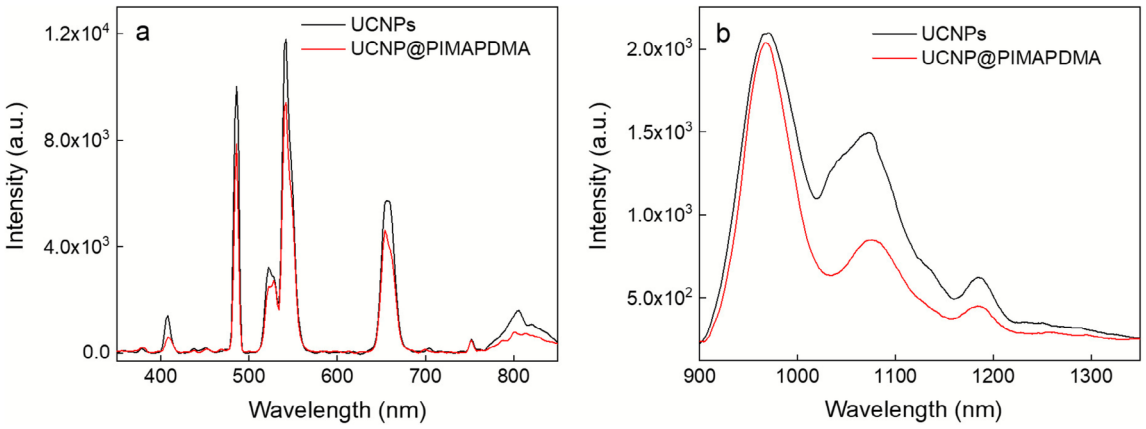

FIGURE 3 | (a) Upconversion and (b) NIR-II emission spectra of aqueous dispersions of UCNPs and UCNP@PIMAPDMA nanoparticles (3 mg/mL) excited at 980 and 735 nm, respectively.

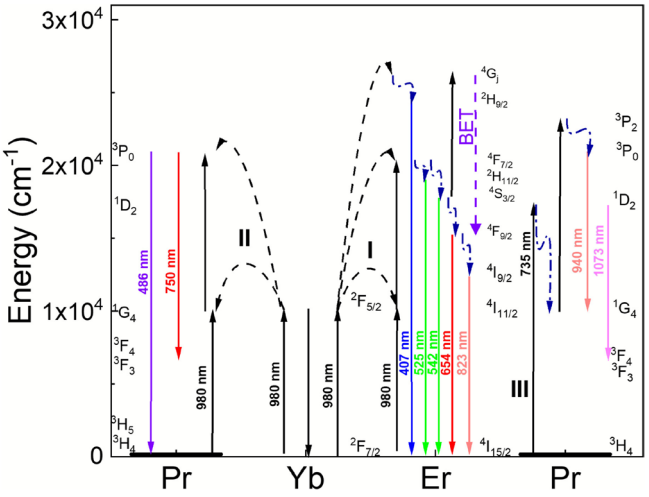

FIGURE 4 | Possible energy transfer of $NaYF_4$:Yb,Er,Pr UCNPs excited at 980 nm (I, II) and 735 nm (III). Only relevant energy levels with radiative (solid straight arrow) and non-radiative transitions (blue dashed curved arrow) are shown. The black dashed curved arrows represent the energy transfer processes between the excited Yb^{3+} ion and the neighboring Er^{3+} (I) and Pr^{3+} ions (II). BET—back energy transfer. The NIST atomic spectra database was used to identify the spectra and energy levels of the spectral lines [45].

of amide. The peaks at 1354, 1400, 2932 and 2868 cm^{-1} were assigned to the $\delta(CH_3)$, $\delta(CH_2)$, $\nu_{as}(CH_3)$ and $\nu_s(CH_2)$ vibrations, respectively. The bands at 1615 and 1730 cm^{-1} corresponded to the vibrations of the $\nu_s(C{=}O)$ in amide and carboxyl, respectively. The broad peak at ~3400 cm^{-1} was attributed to the ν(OH) and ν(NH) vibrations. In the spectrum of UCNP@PIMAPDMA, the new band at 1114 cm^{-1} was assigned to the $\nu_{as}(P{-}O)$ vibration of PO_3^{2-} group due to its coordination to metal ions on the particle surface. The peaks at 1638 and 1702 cm^{-1} were attributed to the $\nu_s(C{=}O)$ in amide and carboxyl groups, respectively. The ν(OH) and ν(NH) vibrations corresponded to the broad band at ~3390 cm^{-1}. These findings were confirmed by XPS analysis of neat UNCPs and UCNP@PIMAPDMA nanoparticles (Figure S6; Table S1). The high-resolution spectrum C 1s of neat UNCPs confirmed the presence of oleic acid with a dominant C—C contribution at 285.0 eV and a minor C(=O)—O contribution at ~289 eV. The neat UCNPs showed a dominating Y 3d and minor Yb peaks in the region between 100 and 240 eV. The binding of the polymer on the surface of UCNP@PIMAPDMA nanoparticles led to significant changes of the high resolution spectra in the C 1s region and the appearance of peaks originating from C—N, C—O, C—S and C—P at 286.2 eV, amide C(=O)—NH at 287.9 eV and carboxyl C(=O)—O at 289.0 eV. At the same time, the presence of PIMAPDMA was associated with the appearance of new NH—C(=O) peaks at 399.8 eV and $C{-}NH_3^+$ at 401.6 eV in high-resolution spectra taken in the N 1s region. Further verification of the presence of PIMAPDMA on the particle surface could be seen in the appearance of the new PO_3 peak at 133.2 eV. In the thermogram of UCNP@PIMAPDMA nanoparticles, the weight loss up to 120°C and in the range of 120°C–560°C was due to the evaporation of adsorbed water and decomposition of the polymer shell. According to TGA, the UCNP@PIMAPDMA nanoparticles contained ~11 wt% of coating (Figure S5b). Thus, FTIR spectroscopy and TGA confirmed the presence of PIMAPDMA on the particle surface.

TEM image of UCNP@PIMAPDMA nanoparticles showed larger particle size and slightly wider particle size distribution ($Đ = 1.04$) compared to neat UCNPs (Figure 2b). PIMAPDMA was visible in the micrograph with lower contrast than inorganic particles and its thickness was estimated to be 4.5 nm (Table 1). The hydrodynamic diameter of the UCNP@PIMAPDMA nanoparticles in water decreased slightly ($D_h = 156$ nm) compared to neat UCNPs ($D_h = 164$ nm), demonstrating the improved stabilization due to the polymer shell, as also documented by the low polydispersity value ($PD = 0.10$), indicating the narrow size distribution of coated particles (Table 1). The ζ-potential of UCNP@PIMAPDMA nanoparticles was negative (−34 mV) due to the presence of bisphosphonate and carboxyl groups of the polymer on the particle surface. The PIMAPDMA coating of UCNPs slightly decreased the emission intensity in both the visible and NIR ranges (Figure 3).

3.3 | Colloidal Stability of UCNP@PIMAPDMA Nanoparticles

The colloidal stability of UCNP@PIMAPDMA nanoparticles in water, PBS, DMEM, and ALF was evaluated by measuring their hydrodynamic diameter D_h and ζ-potential at 37°C and compared with neat particles (Figure 5a,b). The ζ-potential was determined only in water due to the interference of components (e.g., amino acids, salts and vitamins) of other media with DLS measurements. The D_h of UCNP@PIMAPDMA nanoparticles in water, DMEM and ALF did not change significantly for at least 7 days; thus, these particles were colloidally stable, that is did not aggregate, suggesting that they were well sterically stabilized. In PBS, the D_h of UCNP@PIMAPDMA nanoparticles did not change for 3 days, indicating a significant improvement in colloidal stability compared to neat UCNPs, which collapsed immediately after contact with the buffer (Figure 5a). It was only after 3 days that the UCNP@PIMAPDMA particle size increased. In the case of the ζ-potential of both positively charged neat UCNPs and negatively charged UCNP@PIMAPDMA nanoparticles in water, no significant changes were observed even after 7 days due to electrostatic repulsions (Figure 5b). Thus, it can be concluded that the PIMAPDMA coating provided excellent colloidal stability of UCNPs in all tested media for at least 3 days, which is long enough for most bioapplications.

3.4 | Degradability of UCNP@PIMAPDMA Nanoparticles

Recent studies have shown that lanthanide-based UCNPs are prone to dissolution in aqueous media due to the solubility of $NaYF_4$, particularly at elevated temperatures. This can lead to a decrease in luminescence intensity and induce cell death [59, 60]. Therefore, the chemical stability of neat UCNPs and UCNP@PIMAPDMA nanoparticles in different media (water, PBS, DMEM, and ALF) was evaluated at 37°C simulating the temperature used in in vivo experiments (Figure 5c). As expected, the particles exhibited the lowest dissolution in water and the highest in PBS due to the accelerated hydrolysis caused by the complexation of the lanthanides with phosphate ions from PBS [61]. In water, the chemical stability of UCNP@PIMAPDMA ($X_F = \sim 1.6$ mol%) was improved, compared to UCNPs ($X_F = 7.2$ mol%). In DMEM and ALF, a major decrease

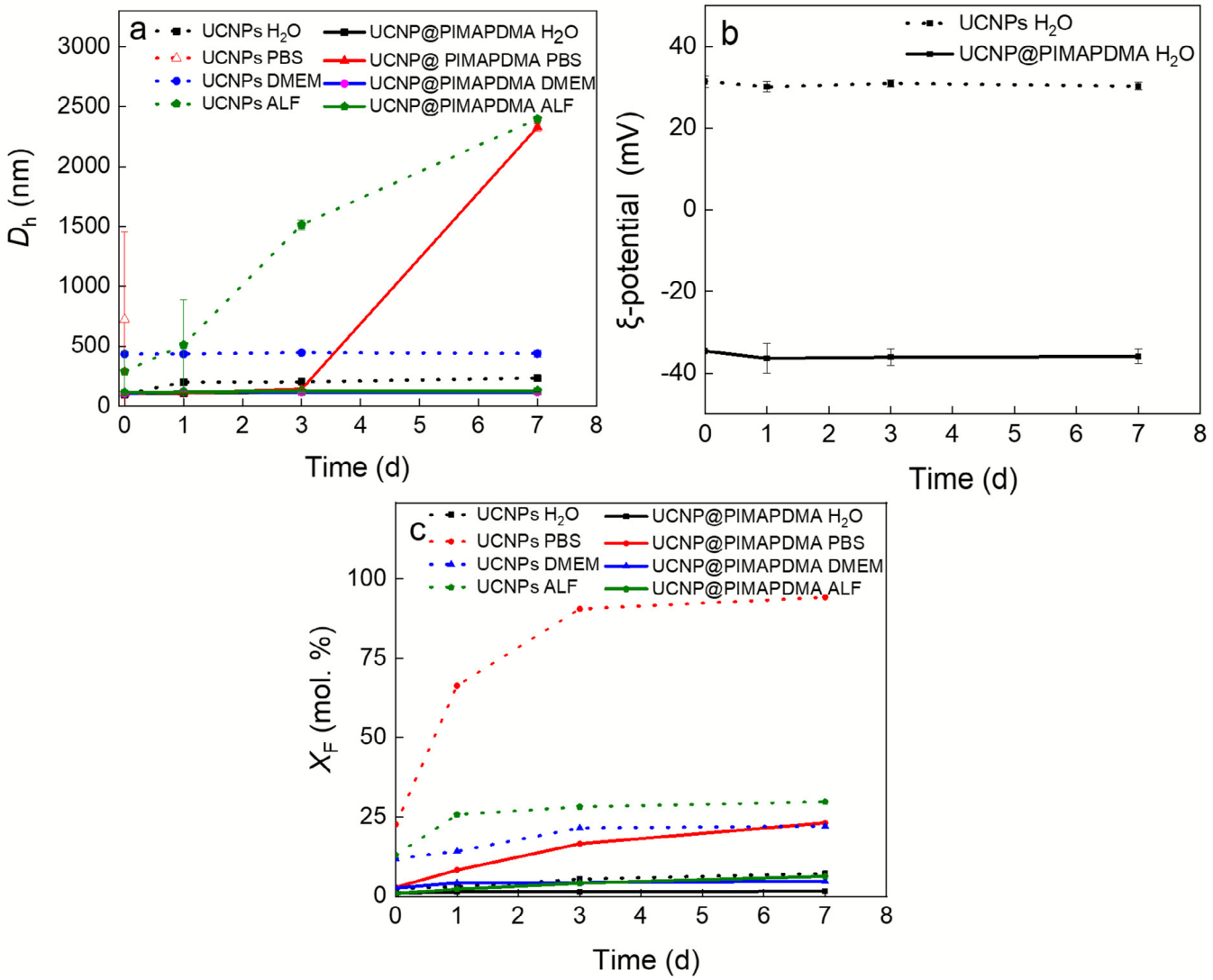

FIGURE 5 | Time dependencies of (a) hydrodynamic diameter D_h in various media, (b) ζ-potential of UCNPs and UCNP@PIMAPDMA nanoparticles in water, and (c) F^- ion molar fraction (X_F) in the supernatants after incubation of particles in water, PBS (pH 7.4), DMEM, and ALF at 37°C.

in dissolution rates of polymer-coated UCNPs was observed ($X_F = 4.7$ and 6.3 mol%, respectively) compared to the neat ones ($X_F = 22$ and 29.8 mol%, respectively). The biggest chemical stability improvement (75% relative to neat UCNPs) was observed in PBS, where the dissolution rate decreased from $X_F = 94$ to 23 mol%; these results are even better (by ~35%) than those published earlier [55, 62]. This can be explained by the effective protection of the surface of UCNPs by PIMAPDMA bound by many phosphonate groups, thus hindering the diffusion of phosphates from PBS. This type of coating therefore ensures good chemical stability of UCNPs and can be used in bioapplications, especially where phosphorus-containing media are required.

3.5 | In Vitro and In Vivo Biological Experiments

The biocompatibility and biosafety of UCNPs and UCNP@PIMAPDMA nanoparticles were assessed in vitro with cultured HEK293 cells using MTT assay and also in in vivo experiments after intravenous injection of particles to laboratory mice. HEK 293 cells were selected because they are considered pseudonormal and are widely used by many researchers as a standard cell line (negative control) when investigating anti-tumor activity [63]. To evaluate the cytotoxicity of particles in vitro, the viability of human embryonic kidney HEK293 cells was measured after treatment with neat UCNPs and UCNP@PIMAPDMA nanoparticles. The results were compared with those of 0.5 μM doxorubicin (Dox) used as a positive control of high toxicity.

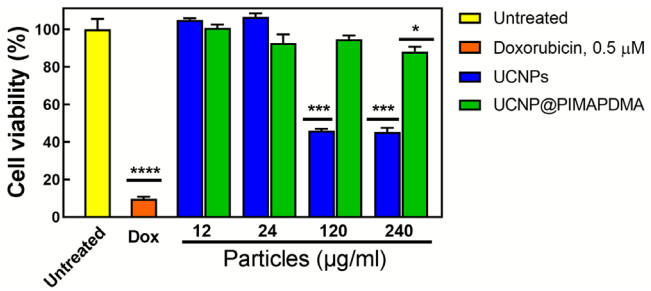

FIGURE 6 | Viability of HEK293 cells incubated with UCNPs and UCNP@PIMAPDMA nanoparticles at a concentration of 12, 24, 120, and 240 μg/mL for 72 h. 0.5 μM doxorubicin (Dox) was used as a positive control, and untreated cells served as a negative control. *$p < 0.05$, ***$p < 0.001$, and ****$p < 0.0001$.

Low concentrations of nanoparticles (12 and 24 μg/mL) were non-toxic for HEK293 cells (Figure 6). However, a distinct toxic effect was observed when these cells were treated with neat UCNPs at doses of 120 and 240 μg/mL, whereas UCNP@PIMAPDMA nanoparticles administered at ≤120 μg/mL were not cytotoxic and at 240 μg/mL were statistically significantly cytotoxic ($p < 0.05$; Figure 6).

For this reason, the toxicity and biosafety of UCNP@PIMAPDMA nanoparticles were further evaluated in vivo following intravenous administration to mice at a dose of 5 mg/kg; this dose was chosen based on a similar published study [64]. All animals remained physically active during the 2-week experiment. One week after the UCNP@PIMAPDMA injection, only a slight but statistically insignificant decrease in animal body mass was found, which might be due to blood sampling (Figure S7). Body mass then increased within 2 weeks, but again, it was a statistically insignificant difference.

Once the nanoparticles enter the blood circulation of mice, they can interact with blood cells, which can lead to changes in the hematological profile of the blood. It should be noted that 2 weeks after injection of UCNP@PIMAPDMA nanoparticles, there were no statistically significant changes in white or red blood cell counts and hemoglobin levels (Figure 7a–c). Fourteen days after administration of UCNP@PIMAPDMA nanoparticles, there was a statistically significant reduction in platelet count ($p < 0.01$) compared to the control (Figure 7d). This is consistent with the literature, although platelet count data vary [65]. Interestingly, before the start of the experiment (Day 0), this group of animals had lower platelet counts than the control group, but this difference was not statistically significant (data not shown). Similarly, there were no differences in neutrophil, lymphocyte and monocyte counts (Figure 7e–g).

In addition to hematological indicators in the blood of mice intravenously injected with UCNP@PIMAPDMA nanoparticles, selected biochemical markers in the blood serum of treated animals, such as alanine aminotransferase (ALT), aspartate aminotransferase (AST) and alkaline phosphatase (ALP), which are enzymatic markers of hepatic injury [66], were examined (Figure S8). In particular, an increased serum ALP activity is an indicator of hepatobiliary damage in humans and experimental animals [67]. Most nephrotoxic agents increase blood urea and serum creatinine, which is a more precise marker of renal toxicity than blood urea because it is not affected by diet [68]. No changes in the levels of enzymatic indicators of hepatotoxicity were observed in mice treated with UCNP@PIMAPDMA nanoparticles (Figure S8a–c). However, a statistically significant reduction in urea content was observed (Figure S8d), whereas serum creatinine levels remained unchanged (Figure S8e), suggesting that the nanoparticles had no nephrotoxic effects [69, 70]. However, other much more specific biochemical markers of hepatotoxicity, namely the activities of AST, ALT and ALP were not affected by the UCNP@PIMAPDMA nanoparticles (Figure S8a–c).

In a previous investigation, specific coatings of magnetic nanoparticles such as poly(*N,N*-dimethylacrylamide) and SiO_2 had a positive effect on the biocompatibility in vivo [41], similar to PIMAPDMA in this study. When comparing toxicity in in vivo and in vitro studies, differences in both types of experiments should be considered. Although in vitro assays are influenced by the conditions of the culture medium, the protein content in the animal's bloodstream is significantly higher than in the culture medium. This may influence the formation of a protein corona around the particles and, thus, their biocompatibility [71]. This hypothesis was tested by incubating UCNP@PIMAPDMA nanoparticles with FBS and detecting changes in the attached proteins using Amido Black 10B dye. Indeed, after incubation with FBS, a distinct protein corona was detected on the particles (Figure 8), confirming that the interaction of particles with blood plasma proteins can affect their biocompatibility.

3.6 | Biological Application

To confirm the potential of the newly developed UCNP@PIMAPDMA nanoparticles for bioimaging, rat C6 glioblastoma cells and rMSC primary were selected as the tumor cell line model and primary culture cells, respectively. After incubation of C6 cells and rMSCs with the particles, both neat UCNPs and UCNP@PIMAPDMA nanoparticles were localized in the cytoplasm (Figure 9); however, the latter particles were more internalized because they did not aggregate.

Emission spectra obtained by lambda scans of rMSCs incubated with nanoparticles had two main emission peaks (542 and 654 nm; Figure 10), similar to previously measured spectra of aqueous dispersions of UCNPs and UCNP@PIMAPDMA nanoparticles (Figure 3a). However, the ratio of intensities of these two peaks differed for various regions of interest (ROIs) represented by different colors and intensities in the cells (Figure 10), as indicated by the different ratio of green and red colors in the overlay images (Figure 9). This ratio appeared to be related to the overall intensity of the signal in the given pixel; the higher the intensity, the stronger the red signal (654 nm) compared to the green signal (542 nm). This can be explained by the larger number of aggregated nanoparticles, which transfer energy more efficiently between neighboring nanoparticles, leading to greater amplification of red emission than green. Several other factors, such as the local cellular environment, pH, ion concentration, and protein interactions, cannot be overlooked, as they can alter the optical properties of UCNPs. Energy transfer processes, such as Förster resonance and different upconversion efficiencies, may also play a role [72]. Understanding these factors is crucial for accurate interpretation of bioimaging results using UCNPs. Nevertheless, due to the zero cellular and tissue background for the combination of excitation and detection settings used, the unique emission patterns of the nanoparticles allow unambiguous localization of UCNPs in vivo.

Last but not least, it should be noted that, in general, further improvement of cell visualization using UCNPs requires optimization of particle composition, including the introduction of a passive shell that prevents quenching and increases luminescence. In addition, it is important to optimize and test the biodegradable polymer coating surrounding the nanoparticles and the conjugation of other bioactive species. This will

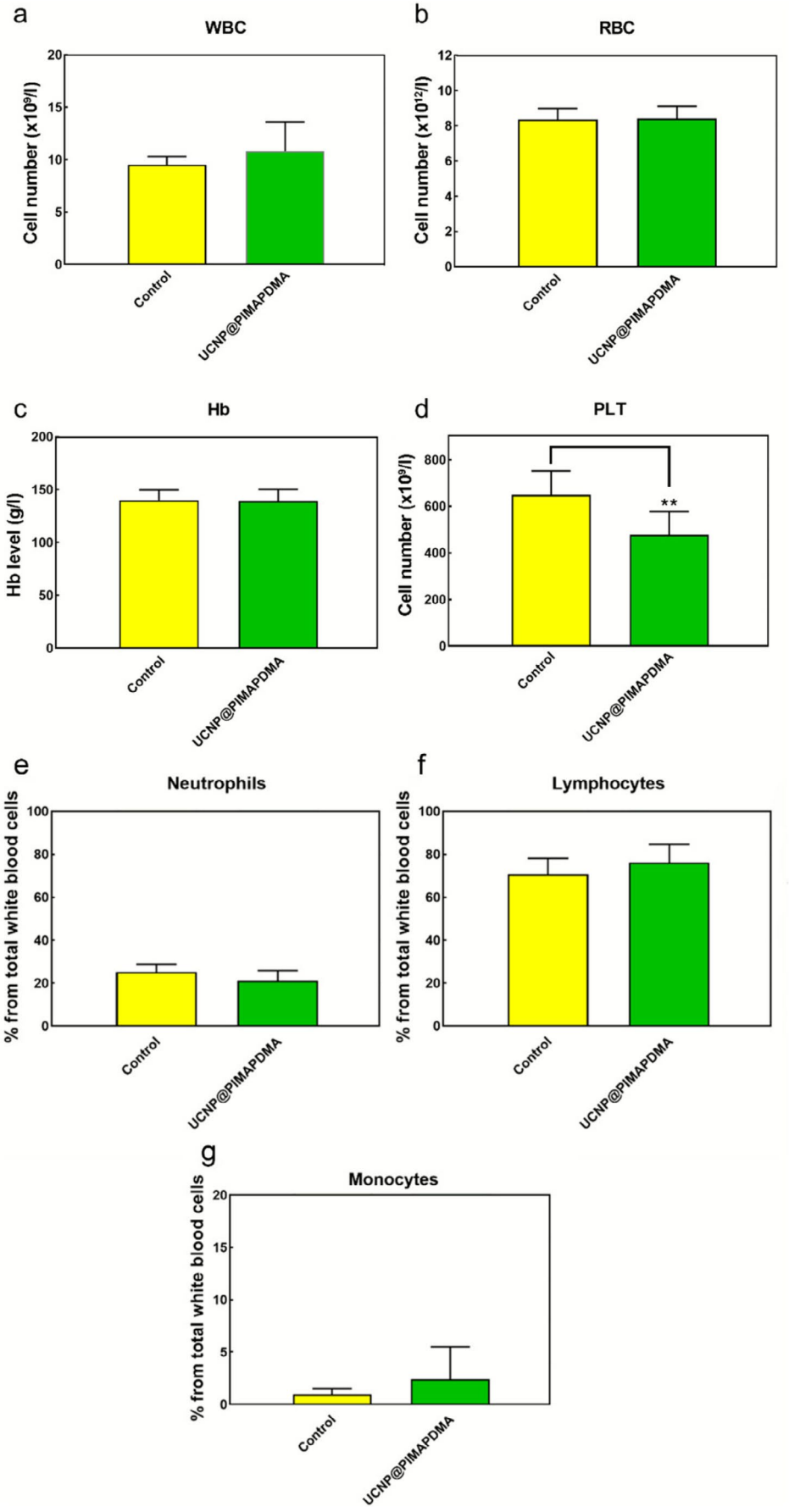

FIGURE 7 | Legend on next page.

FIGURE 7 | Concentration of (a) white blood cells (WBC), (b) red blood cells (RBC), (c) hemoglobin (Hb), (d) platelets (PLT), (e) neutrophils, (f) lymphocytes, and (g) monocytes in the blood of mice 2 weeks after intravenous administration of UCNP@PIMAPDMA nanoparticles. The yellow and green symbols represent blood parameters of individual animals. $^{**}p < 0.01$.

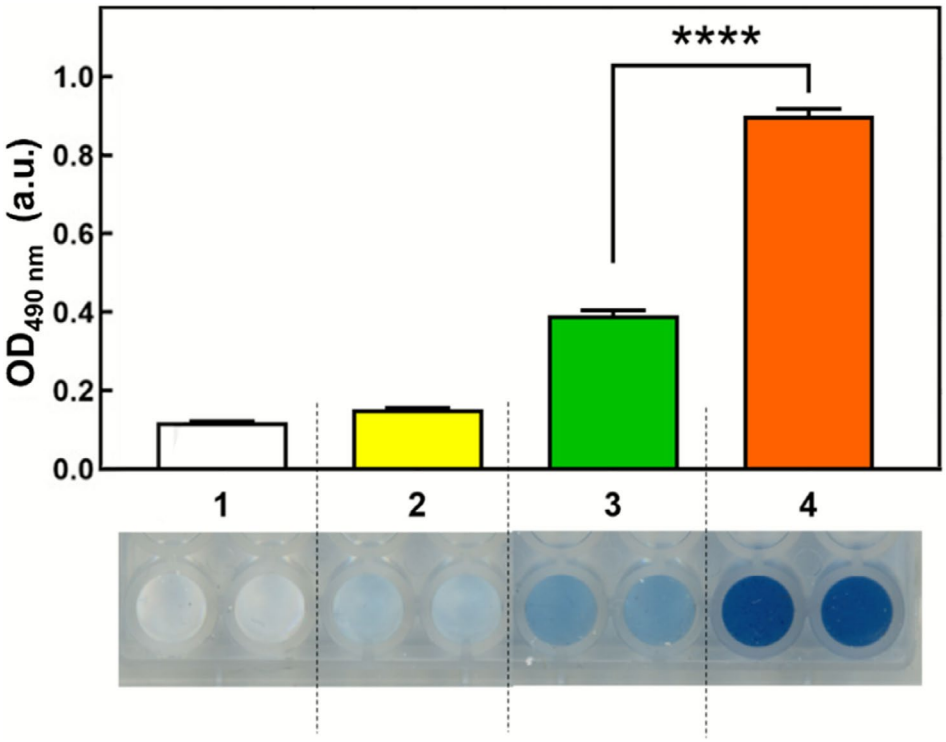

FIGURE 8 | Detection of protein corona after UCNP@PIMAPDMA nanoparticle staining with Amido Black 10B. (1) negative control (Amido Black 10B), (2) fetal bovine serum (FBS), (3) UCNP@PIMAPDMA and (4) UCNP@PIMAPDMA and FBS. The bottom photo shows a microplate containing a dispersion of particles after staining with Amido Black 10B dye. $^{****}p < 0.0001$.

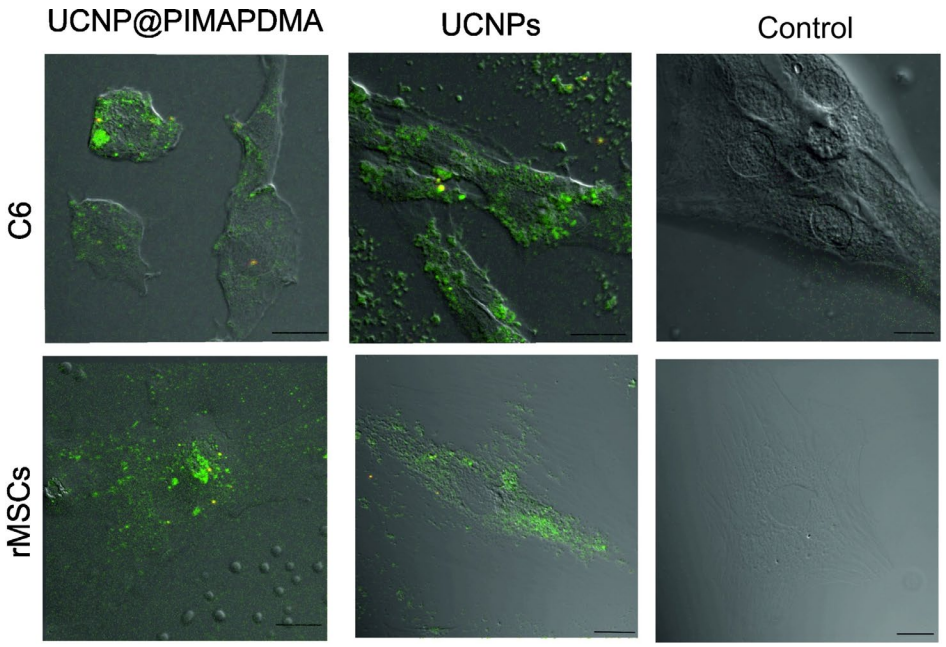

FIGURE 9 | Laser scanning micrographs of C6 cells and rMSCs incubated with UCNPs and UCNP@PIMAPDMA nanoparticles for 2 days overlaid with DIC images; green (535–561 nm) and red channel (641–686 nm) overlay; excitation at 975 nm. Cells not incubated with nanoparticles served as a control. Scale bar 20 μm.

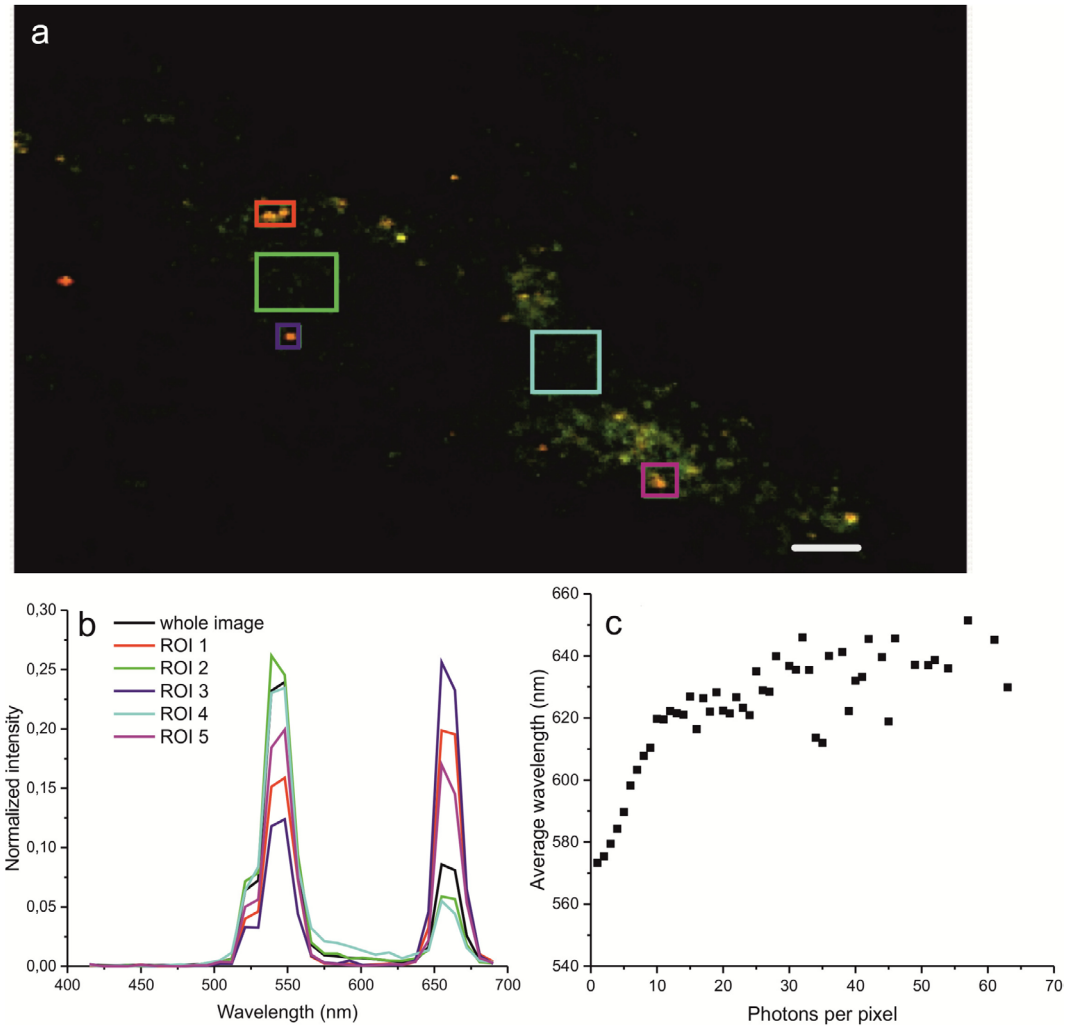

FIGURE 10 | (a) 32 channel spectral image of rMSCs labeled with UCNPs. The color encodes the real spectrum. (b) Emission spectra from the whole image (black) and from selected regions of interest (ROIs in color) showing the ratio of intensity variability between the main emission peaks of UNCPs. (c) Relation between signal intensity (expressed as photons per pixel) and spectral shift (expressed as the average wavelength); the higher the local emitted intensity, the higher 654 nm red peak emission. Scale bar 50 μm.

ensure selectivity and targeting of specific cells, expanding the therapeutic possibilities of the particles and their overall applicability.

4 | Conclusions

Yb^{3+}, Er^{3+} and Pr^{3+}-doped upconversion nanoparticles were successfully synthesized by the high-temperature coprecipitation method. After excitation at 980 and 735 nm, the UCNPs exhibited bright blue, green and red luminescence in the form of narrow peaks in the range of ~480–700 nm in the visible part of the spectrum, as well as emission bands in the NIR-II region of the spectrum (> 1000 nm). Achieving luminescence emission simultaneously in the visible and NIR-II regions is rather rarely described in the literature. Although downshifting emission is more suitable for cell imaging, upconversion is applicable for deep tissue imaging. Thus, the excellent luminescence emission efficiency in the visible-to-NIR-II region holds promise for the use of such particles in biotherapy and imaging. In biomedical in vivo applications, injected UCNPs should have a limited retention time in the body without accumulating permanently, and at the same time should not cause undesirable chronic reactions resulting from their dissolution and release of lanthanide ions. To ensure the biocompatibility of the UCNPs and establish their future degradability, the nanoparticles were coated with a bisphosphonate-modified copolymer based on poly(isobutylene-*alt*-maleic acid) and poly(*N,N*-dimethylacrylamide) containing degradable disulfide bonds. Such a coating provided significantly higher colloidal and chemical stability of particles in PBS than previously investigated coatings due to a larger number of phosphonate anchoring groups attached to the UCNP surface [55]. In addition, various bioactive substances, including drugs, can be immobilized on such coated particles by reacting the available functional amino and carboxyl groups of the polymer, which allows for the design of new drug delivery systems. The biocompatibility of the newly developed UCNP@PIMAPDMA nanoparticles towards cultured human embryonic kidney HEK293 cells and the biosafety after intravenous administration to experimental mice suggested the great potential of these particles for tissue bioimaging. This was successfully demonstrated when the particles were detected in the cytoplasm of rMSCs and

C6 glioblastoma rat cells by laser scanning confocal microscopy, confirming efficient particle uptake.

Author Contributions

The manuscript was written through the contributions of all authors. All authors have given approval to the final version of the manuscript. T.V. synthesis of particles. S.P. in vitro experiments. T.D. coordination of biological experiments. V.S. biochemical analysis. N.S. protein adsorption tests. O.K. cell viability evaluation. V.P. synthesis of polymers. R.K. ^{1}H NMR analysis. J.H. TEM micrographs. O.S. modification of particles. L.M.U. cell imaging. D.M. cell culture experiments. A.B. confocal microscopy. P.J. biological experiments. O.P.-G. XPS analysis. R.S. description of biological results. D.H. writing of manuscript.

Acknowledgments

The authors acknowledge the financial support of the Czech Science Foundation (No. 24-10125S), the help of Cedars-Sinai Medical Center's International Research and Innovation in Medicine Program and the RECOOP HST Association and Imaging Methods Core Facility at BIOCEV, institution supported by the MEYS CR (LM2023050 Czech-BioImaging) for their support with cellular imaging. Open access publishing facilitated by Ustav makromolekularni chemie Akademie ved Ceske republiky, as part of the Wiley - CzechELib agreement.

Funding

This work was supported by Grantová Agentura České Republiky (24-10125S), RECOOP HST Association, Ministerstvo Školství, Mládeže a Tělovýchovy (LM2023050).

Conflicts of Interest

The authors declare no conflicts of interest.

Data Availability Statement

The data that support the findings of this study are available from the corresponding author upon reasonable request.

References

1. E. Andresen, F. Islam, C. Prinz, et al., "Assessing the Reproducibility and Up-Scaling of the Synthesis of Er,Yb-Doped $NaYF_4$-Based Upconverting Nanoparticles and Control of Size, Morphology, and Optical Properties," *Scientific Reports* 13 (2023): 2288, https://doi.org/10.1038/s41598-023-28875-8.

2. J. Guo, H. Yu, and T. Cui, "Applications of Fluorescent Materials in the Detection of Alkaline Phosphatase Activity," *Journal of Biomedical Materials Research Part B: Applied Biomaterials* 109 (2021): 214–226, https://doi.org/10.1002/jbm.b.34693.

3. N. Feliu, J. Hühn, M. V. Zyuzin, et al., "Quantitative Uptake of Colloidal Particles by Cell Cultures," *Science of the Total Environment* 568 (2016): 819–828, https://doi.org/10.1016/j.scitotenv.2016.05.213.

4. A. Escudero, A. I. Becerro, C. Carrillo-Carrión, et al., "Rare Earth Based Nanostructured Materials: Synthesis, Functionalization, Properties and Bioimaging and Biosensing Applications," *Nano* 6 (2017): 881–921, https://doi.org/10.1515/nanoph-2017-00075.

5. S. P. Tiwari, S. K. Maurya, R. S. Yadav, et al., "Future Prospects of Fluoride Based Upconversion Nanoparticles for Emerging Applications in Biomedical and Energy Harvesting," *Journal of Vacuum Science & Technology B* 36 (2018): 060801, https://doi.org/10.1116/1.5044596.

6. Q. Fan, X. Cui, Q. Wang, et al., "A Novel Photostable Near-Infrared-To-Near-Infrared Fluorescent Nanoparticle for In Vivo Imaging," *Journal of Biomedical Materials Research. Part B, Applied Biomaterials* 108B (2020): 2912–2924, https://doi.org/10.1002/jbm.b.34622.

7. R. Lv, M. Raab, Y. Wang, J. Tian, J. Lin, and P. N. Prasad, "Nanochemistry Advancing Photon Conversion in Rare-Earth Nanostructures for Theranostics," *Coordination Chemistry Reviews* 460 (2022): 214486, https://doi.org/10.1016/j.ccr.2022.214486.

8. R. Lv, Y. Wang, B. Lin, et al., "Targeted Luminescent Probes for Precise Upconversion/NIR II Luminescence Diagnosis of Lung Adenocarcinoma," *Analytical Chemistry* 93 (2021): 4984–4992, https://doi.org/10.1021/acs.analchem.1c00374.

9. M. Y. Tsang, P. Fałat, M. A. Antoniak, et al., "Pr^{3+} Doped $NaYF_4$ and $LiYF_4$ Nanocrystals Combining Visible-To-UVC Upconversion and NIR-To-NIR-II Downconversion Luminescence Emissions for Biomedical Applications," *Nanoscale* 14 (2022): 14770–14778, https://doi.org/10.1039/d2nr01680j.

10. G. Yi, H. Lu, S. Zhao, et al., "Synthesis, Characterization, and Biological Application of Size-Controlled Nanocrystalline $NaYF_4$:Yb,Er Infrared-To-Visible Up-Conversion Phosphors," *Nano Letters* 4 (2004): 2191–2196, https://doi.org/10.1021/nl048680h.

11. R. Rafique, S. H. Baek, L. M. T. Phan, S.-J. Chang, A. R. Gul, and T. J. Park, "A Facile Hydrothermal Synthesis of Highly Luminescent $NaYF_4$:Yb^{3+}/Er^{3+} Upconversion Nanoparticles and Their Biomonitoring Capability," *Materials Science and Engineering: C* 99 (2019): 1067–1074, https://doi.org/10.1016/j.msec.2019.02.046.

12. I. Halimi, E. M. Rodrigues, S. L. Maurizio, et al., "Pick Your Precursor! Tailoring the Size and Crystal Phase of Microwave-Synthesized Sub-10 Nm Upconverting Nanoparticles," *Journal of Materials Chemistry C* 7 (2019): 15364–15374, https://doi.org/10.1039/c9tc04817k.

13. B. Chen, W. Kong, N. Wang, G. Zhu, and F. Wang, "Oleylamine-Mediated Synthesis of Small $NaYbF_4$ Nanoparticles With Tunable Size," *Chemistry of Materials* 31 (2019): 4779–4786, https://doi.org/10.1021/acs.chemmater.9b01050.

14. X. Ye, J. E. Collins, Y. Kang, et al., "Morphologically Controlled Synthesis of Colloidal Upconversion Nanophosphors and Their Shape-Directed Self-Assembly," *Proceedings of the National Academy of Sciences* 107 (2010): 22430–22435, https://doi.org/10.1073/pnas.1008958107.

15. M. V. Zyuzin, T. Honold, S. Carregal-Romero, K. Kantner, M. Karg, and W. J. Parak, "Influence of Temperature on the Colloidal Stability of Polymer-Coated Gold Nanoparticles in Cell Culture Media," *Small* 12 (2016): 1723–1731, https://doi.org/10.1002/smll.201503232.

16. B. Li, A. A. Ansari, A. K. Parchur, and R. Lv, "Exploring the Influence of Polymeric and Non-Polymeric Materials in Synthesis and Functionalization of Luminescent Lanthanide Nanomaterials," *Coordination Chemistry Reviews* 514 (2024): 215922, https://doi.org/10.1016/j.ccr.2024.215922.

17. M. H. Stewart, K. Susumu, B. C. Mei, et al., "Multidentate Poly(Ethylene Glycol) Ligands Provide Colloidal Stability to Semiconductor and Metallic Nanocrystals in Extreme Conditions," *Journal of the American Chemical Society* 132 (2010): 9804–9813, https://doi.org/10.1021/ja102898d.

18. Y. Que, C. Feng, G. Lu, and X. Huang, "Polymer-Coated Ultrastable and Biofunctionalizable Lanthanide Nanoparticles," *ACS Applied Materials & Interfaces* 9 (2017): 14647–14655, https://doi.org/10.1021/acsami.7b01452.

19. S. Chairam and E. Somsook, "Starch Vermicelli Template for Synthesis of Magnetic Iron Oxide Nanoclusters," *Journal of Magnetism and Magnetic Materials* 320 (2008): 2039–2043, https://doi.org/10.1016/j.jmmm.2008.02.168.

20. C. C. Berry, S. Wells, S. Charles, and A. S. G. Curtis, "Dextran and Albumin Derivatised Iron Oxide Nanoparticles: Influence on Fibroblasts

In Vitro," *Biomaterials* 24 (2003): 4551–4557, https://doi.org/10.1016/S0142-9612(03)00237-0.

21. J.-H. Park, K.-H. Im, S.-H. Lee, et al., "Preparation and Characterization of Magnetic Chitosan Particles for Hyperthermia Application," *Journal of Magnetism and Magnetic Materials* 293 (2005): 328–333, https://doi.org/10.1016/j.jmmm.2005.02.027.

22. M. Longmire, P. L. Choyke, and H. Kobayashi, "Clearance Properties of Nano-Sized Particles and Molecules as Imaging Agents: Considerations and Caveats," *Nanomedicine* 3 (2008): 703–717, https://doi.org/10.2217/17435889.3.5.703.

23. W. Wu, Q. He, and C. Jiang, "Magnetic Iron Oxide Nanoparticles: Synthesis and Surface Functionalization Strategies," *Nanoscale Research Letters* 3 (2008): 397–415, https://doi.org/10.1007/s11671-008-9174-9.

24. H. S. Park, G. Dodbiba, L. F. Cao, and T. Fujita, "Synthesis of Silica-Coated Ferromagnetic Fine Powder by Heterocoagulation," *Journal of Physics. Condensed Matter* 20 (2008): 204105, https://doi.org/10.1088/0953-8984/20/20/204105.

25. K. S. Sharma, A. K. Dubey, C. Kumar, P. P. Phadnis, V. Sudarsan, and R. K. Vatsa, "Mesoporous Silica-Coated Upconversion Nanoparticles Assisted Photodynamic Therapy Using 5-Aminolevulinic Acid: Mechanistic and In Vivo Studies," *ACS Applied Bio Materials* 5 (2022): 583–597, https://doi.org/10.1021/acsabm.1c01074.

26. N. Pazos-Pérez, Y. Gao, M. Hilgendorff, et al., "Magnetic–Noble Metal Nanocomposites With Morphology-Dependent Optical Response," *Chemistry of Materials* 19 (2007): 4415–4422, https://doi.org/10.1021/cm070248o.

27. D. V. Talapin, A. L. Rogach, A. Kornowski, M. Haase, and H. Weller, "Highly Luminescent Monodisperse CdSe and CdSe/ZnS Nanocrystals Synthesized in a Hexadecylamine-Trioctylphosphine Oxide-Trioctylphospine Mixture," *Nano Letters* 1 (2001): 207–211, https://doi.org/10.1021/nl0155126.

28. Y. Sahoo, H. Pizem, T. Fried, et al., "Alkyl Phosphonate/Phosphate Coating on Magnetite Nanoparticles: A Comparison With Fatty Acids," *Langmuir* 17 (2001): 7907–7911, https://doi.org/10.1021/la010703+.

29. B. Liu, Y. Chen, C. Li, et al., "Poly(Acrylic Acid) Modification of Nd^{3+}-Sensitized Upconversion Nanophosphors for Highly Efficient UCL Imaging and pH-Responsive Drug Delivery," *Advanced Functional Materials* 25 (2015): 4717–4729, https://doi.org/10.1002/adfm.201501582.

30. J. C. Boyer, N. J. J. Johnson, and F. C. J. M. van Veggel, "Upconverting Lanthanide-Doped $NaYF_4$–PMMA Polymer Composites Prepared by In Situ Polymerization," *Chemistry of Materials* 21 (2009): 2010–2012, https://doi.org/10.1021/cm900756h.

31. G. Liu, Z. Sun, Z. Fu, L. Ma, and X. Wang, "Temperature Sensing and Bio-Imaging Applications Based on Polyethylenimine/CaF_2 Nanoparticles With Upconversion Fluorescence," *Talanta* 169 (2017): 181–188, https://doi.org/10.1016/j.talanta.2017.03.054.

32. G. Jiang, J. Pichaandi, N. J. J. Johnson, R. D. Burke, and F. C. J. M. van Veggel, "An Effective Polymer Cross-Linking Strategy to Obtain Stable Dispersions of Upconverting $NaYF_4$ Nanoparticles in Buffers and Biological Growth Media for Biolabeling Applications," *Langmuir* 28 (2012): 3239–3247, https://doi.org/10.1021/la204020m.

33. T. Pellegrino, L. Manna, S. Kudera, et al., "Hydrophobic Nanocrystals Coated With an Amphiphilic Polymer Shell: A General Route to Water Soluble Nanocrystals," *Nano Letters* 4 (2004): 703–707, https://doi.org/10.1021/nl035172j.

34. M.-S. Martina, J.-P. Fortin, C. Ménager, et al., "Generation of Superparamagnetic Liposomes Revealed as Highly Efficient MRI Contrast Agents for In Vivo Imaging," *Journal of the American Chemical Society* 127 (2005): 10676–10685, https://doi.org/10.1021/ja0516460.

35. S. Campora and G. Ghersi, "Recent Developments and Applications of Smart Nanoparticles in Biomedicine," *Nanotechnology Reviews* 11 (2022): 2595–2631, https://doi.org/10.1515/ntrev-2022-0148.

36. K. Malhotra, R. Fuku, B. Kumar, et al., "Unlocking Long-Term Stability of Upconversion Nanoparticles With Biocompatible Phosphonate-Based Polymer Coatings," *Nano Letters* 22 (2022): 7285–7293, https://doi.org/10.1021/acs.nanolett.2c00437.

37. S. Shiva, A. Prabu, G. Bajaj, et al., "A Review on the Recent Applications of Synthetic Biopolymers in 3D Printing for Biomedical Applications," *Journal of Materials Science. Materials in Medicine* 34 (2023): 62, https://doi.org/10.1007/s10856-023-06765-9.

38. C. Colombo, A. J. Monhemius, and J. A. Plant, "Platinum, Palladium and Rhodium Release From Vehicle Exhaust Catalysts and Road Dust Exposed to Simulated Lung Fluids," *Ecotoxicology and Environmental Safety* 71 (2008): 722–730, https://doi.org/10.1016/j.ecoenv.2007.11.011.

39. V. Oleksa, H. Macková, V. Patsula, A. Dydowiczová, O. Janoušková, and D. Horák, "Doxorubicin-Conjugated Iron Oxide Nanoparticles: Surface Engineering and Biomedical Investigation," *ChemPlusChem* 85 (2020): 1156–1163, https://doi.org/10.1002/cplu.202000360.

40. H. Li, H. Jiang, M. Zhao, Y. Fua, and X. Sun, "Intracellular Redox Potential-Responsive Micelles Based on Polyethylenimine-Cystamine-Poly(ε-Caprolactone) *Block* Copolymer for Enhanced miR-34a Delivery," *Polymer Chemistry* 6 (2015): 1952–1960, https://doi.org/10.1039/C4PY01623H.

41. S. Paryzhak, T. Dumych, B. Zasońska, et al., "Improvement of Hemocompatibility of γ-Fe_2O_3 Nanoparticles via Their Covering With Complex Poly(*N,N*-Dimethylacrylamide) and SiO_2 Shell," *Applied Nanoscience* 13 (2023): 7399–7412, https://doi.org/10.1007/s13204-023-02905-3.

42. S. Parasuraman, R. Raveendran, and R. Kesavan, "Blood Sample Collection in Small Laboratory Animals," *Journal of Pharmacy and Pharmacology* 1 (2010): 87–93, https://doi.org/10.4103/0976-500X.72350.

43. B. Qiao, S. Zhao, and Y. Zheng, "Synthesis and Preparation of Upconverting Phosphor Particles," in *Principles and Applications of Up-Converting Phosphor Technology*, ed. R. Yang (Springer Nature Singapore, 2019), 33–62.

44. W. A. Pisarski, J. Pisarska, M. Kuwik, et al., "Fluoroindate Glasses Co-Doped With Pr^{3+}/Er^{3+} for Near-Infrared Luminescence Applications," *Scientific Reports* 10 (2020): 21105, https://doi.org/10.1038/s41598-020-77943-w.

45. A. Kramida, Y. Ralchenko, J. Reader, and NIST ASD Team, "NIST Atomic Spectra Database (Ver. 5.11). National Institute of Standards and Technology," 2023 Gaithersburg, MD, USA, https://physics.nist.gov/asd, https://doi.org/10.18434/T4W30F.

46. M. T. Berry and P. S. May, "Disputed Mechanism for NIR-To-Red Upconversion Luminescence in $NaYF_4$:$Yb^{(3+)}$,$Er^{(3+)}$," *Journal of Physical Chemistry A* 119 (2015): 9805–9811, https://doi.org/10.1021/acs.jpca.5b08324.

47. C. Lee, H. Park, W. Kim, and S. Park, "Origin of Strong Red Emission in Er^{3+}-Based Upconversion Materials: Role of Intermediate States and Cross Relaxation," *Physical Chemistry Chemical Physics* 21 (2019): 24026–24033, https://doi.org/10.1039/c9cp04692e.

48. R. B. Anderson, S. J. Smith, P. S. May, and M. T. Berry, "Revisiting the NIR-To-Visible Upconversion Mechanism in β-$NaYF_4$:Yb^{3+}, Er^{3+}," *Journal of Physical Chemistry Letters* 5 (2014): 36–42, https://doi.org/10.1021/jz402366r.

49. P. V. dos Santos, E. A. Gouveia, M. T. Araujo, A. S. de Gouveia-Neto, S. J. L. Ribeiro, and S. H. S. Benedicto, "IR-Visible Upconversion and Thermal Effects in Pr^{3+}/Yb^{3+}-Codoped Ga_2O_3:La_2S_3 Chalcogenide Glasses," *Journal of Physics. Condensed Matter* 12 (2000): 10003–10010, https://doi.org/10.1088/0953-8984/12/48/316.

50. W. Wudi, Y. Xue, J. Dong, et al., "Yb^{3+} Sensitization Effect to Pr^{3+} Originated From $^1G_4$ Level Broadband Near-Infrared Emission and Up-Conversion in BaF_2 Crystal," *Optical Materials Express* 13 (2023): 1267–1277, https://doi.org/10.1364/OME.471546.

51. A. S. Gouveia-Neto, E. B. da Costa, L. A. Bueno, and S. J. L. Ribeiro, "Red, Green, and Blue Upconversion Luminescence in Ytterbium-Sensitized Praseodymium-Doped Lead–Cadmium–Germanate Glass," *Optical Materials* 26 (2004): 271–274, https://doi.org/10.1016/j.optmat.2003.12.012.

52. D. K. Mohanty and V. K. Rai, "Photoluminescence Studies of Pr^{3+} Doped Lead Germanate Glass," *Journal of Fluorescence* 21 (2011): 1455–1460, https://doi.org/10.1007/s10895-010-0830-y.

53. R. Balda, J. Fernández, A. Pablos, and J. M. Fdez-Navarro, "Spectroscopic Properties of Pr^{3+} Ions in Lead Germanate Glass," *Journal of Physics. Condensed Matter* 11 (1999): 7411–7421, https://doi.org/10.1088/0953-8984/11/38/317.

54. L. H. Acioli, A. S. L. Gomes, C. B. de Araújo, and C. N. Ironside, "Infrared-To-Blue Frequency Upconversion in a Pr^{3+}-Doped Silicate Fiber," *Physical Review B* 54 (1996): 9126–9130, https://doi.org/10.1103/physrevb.54.9126.

55. M. Nahorniak, V. Patsula, D. Mareková, et al., "Chemical and Colloidal Stability of Polymer-Coated $NaYF_4$:Yb,Er Nanoparticles in Aqueous Media and Viability of Cells: The Effect of a Protective Coating," *International Journal of Molecular Sciences* 24 (2023): 2724, https://doi.org/10.3390/ijms24032724.

56. M. H. Lee, Z. Yang, C. W. Lim, et al., "Disulfide-Cleavage-Triggered Chemosensors and Their Biological Applications," *Chemical Reviews* 113 (2013): 5071–5109, https://doi.org/10.1021/cr300358b.

57. B. C. Barja and M. dos Santos Afonso, "An ATR-FTIR Study of Glyphosate and Its Fe(III) Complex in Aqueous Solution," *Environmental Science & Technology* 32 (1998): 3331–3335, https://doi.org/10.1021/es9800380.

58. M. C. Zenobi, C. V. Luengo, M. J. Avena, and E. H. Rueda, "An ATR-FTIR Study of Different Phosphonic Acids in Aqueous Solution," *Spectrochimica Acta A* 70 (2008): 270–276, https://doi.org/10.1016/j.saa.2007.07.043.

59. M. I. Saleh, B. Rühle, S. Wang, J. Radnik, Y. You, and U. Resch-Genger, "Assessing the Protective Effects of Different Surface Coatings on $NaYF_4$:Yb^{3+}, Er^{3+} Upconverting Nanoparticles in Buffer and DMEM," *Scientific Reports* 10 (2020): 19318, https://doi.org/10.1038/s41598-020-76116-z.

60. E. Andresen, C. Würth, C. Prinz, M. Michaelis, and U. Resch-Genger, "Time-Resolved Luminescence Spectroscopy for Monitoring the Stability and Dissolution Behavior of Upconverting Nanocrystals With Different Surface Coatings," *Nanoscale* 12 (2020): 12589–12601, https://doi.org/10.1039/D0NR02931A.

61. D. Lisjak, O. Plohl, J. Vidmar, B. Majaron, and M. Ponikvar-Svet, "Dissolution Mechanism of Upconverting AYF_4:Yb,Tm (A = Na or K) Nanoparticles in Aqueous Media," *Langmuir* 32 (2016): 8222–8229, https://doi.org/10.1021/acs.langmuir.6b02675.

62. T. Vasylyshyn, V. Patsula, M. Filipová, R.-L. Konefał, and D. Horák, "Poly(Glycerol Monomethacrylate)-Encapsulated Upconverting Nanoparticles Prepared by Miniemulsion Polymerization: Morphology, Chemical Stability, Antifouling Properties and Toxicity Evaluation," *Nanoscale Advances* 5 (2023): 6979–6989, https://doi.org/10.1039/d3na00793f.

63. X. Liu, K. Shan, X. Shao, et al., "Nanotoxic Effects of Silver Nanoparticles on Normal HEK-293 Cells in Comparison to Cancerous HeLa Cell Line," *International Journal of Nanomedicine* 16 (2021): 753–761, https://doi.org/10.2147/IJN.S289008.

64. L. Xiong, T. Yang, Y. Yang, C. Xu, and F. Li, "Long-Term In Vivo Biodistribution Imaging and Toxicity of Polyacrylic Acid-Coated Upconversion Nanophosphors," *Biomaterials* 31, no. 27 (2010): 7078–7085, https://doi.org/10.1016/j.biomaterials.2010.05.065.

65. G. Silva-Santana, J. C. Bax, D. C. S. Fernandes, et al., "Clinical Hematological and Biochemical Parameters in Swiss, BALB/c, C57BL/6 and B6D2F1 *Mus musculus*," *Animal Models and Experimental Medicine* 3 (2020): 304–315, https://doi.org/10.1002/ame2.12139.

66. Z. Zhang, S. Zhang, F. Zhang, et al., "Clinical Indicators of Hepatotoxicity in Newly Diagnosed Acute Promyelocytic Leukemia Patients Undergoing Arsenic Trioxide Treatment," *Biological Trace Element Research* 202 (2024): 122–132, https://doi.org/10.1007/s12011-023-03676-2.

67. Y. Yokoyama, A. Ono, M. Yoshida, K. Matsumoto, and M. Saito, "Toxicological Significance of Increased Serum Alkaline Phosphatase Activity in Dog Studies of Pesticides: Analysis of Toxicological Data Evaluated in Japan," *Regulatory Toxicology and Pharmacology* 109 (2019): 104482, https://doi.org/10.1016/j.yrtph.2019.104482.

68. M. S. Al-Naimi, H. A. Rasheed, N. R. Hussien, H. M. Al-Kuraishy, and A. I. Al-Gareeb, "Nephrotoxicity: Role and Significance of Renal Biomarkers in the Early Detection of Acute Renal Injury," *Journal of Advanced Pharmaceutical Technology & Research* 10 (2019): 95–99, https://doi.org/10.4103/japtr.JAPTR_336_18.

69. L. A. Inker and A. S. Levey, "Assessment of Glomerular Filtration Rate in Acute and Chronic Settings," in *National Kidney Foundation Primer on Kidney Diseases*, 6th ed., ed. S. J. Gilbert and D. E. Weiner (W.B. Saunders, 2014), 26–32, https://doi.org/10.1016/B978-1-4557-4617-0.00003-0.

70. V. Lala, M. Zubair, and D. A. Minter, "Liver Function Tests," in *StatPearls* (StatPearls Publishing, 2024).

71. G. Bashiri, M. S. Padilla, K. L. Swingle, S. J. Shepherd, M. J. Mitchell, and K. Wang, "Nanoparticle Protein Corona: From Structure and Function to Therapeutic Targeting," *Lab on a Chip* 23 (2023): 1432–1466, https://doi.org/10.1039/d2lc00799a.

72. A. M. Kotulska, A. Pilch-Wróbel, S. Lahtinen, T. Soukka, and A. Bednarkiewicz, "Upconversion FRET Quantitation: The Role of Donor Photoexcitation Mode and Compositional Architecture on the Decay and Intensity Based Responses," *Light: Science & Applications* 11 (2022): 256, https://doi.org/10.1038/s41377-022-00946-x.

Supporting Information

Additional supporting information can be found online in the Supporting Information section. **Data S1:** jbmb70011-sup-0001-Supinfo.docx.